

Gravitational Recoil From Accretion-Aligned Black-Hole Binaries

Carlos O. Lousto, Yosef Zlochower,¹ Massimo Dotti,² and Marta Volonteri³

¹*Center for Computational Relativity and Gravitation,
and School of Mathematical Sciences, Rochester Institute of Technology,
85 Lomb Memorial Drive, Rochester, New York 14623*

²*Università di Milano Bicocca, Dipartimento di Fisica G. Occhialini,
Piazza della Scienza 3, I-20126, Milano, Italy*

³*Astronomy Department, University of Michigan, Ann Arbor 48109,
USA and Institut d'Astrophysique de Paris, 98 bis Bd Arago, Paris, 75014, France*

We explore the newly discovered “hangup-kick” effect, which greatly amplifies the recoil for configurations with partial spin-/ orbital-angular momentum alignment, by studying a set of 48 new simulations of equal-mass, spinning black-hole binaries. We propose a phenomenological model for the recoil that takes this new effect into account and then use this model, in conjunction with statistical distributions for the spin magnitude and orientations, based on accretion simulations, to find the probabilities for observing recoils of several thousand km s^{-1} . In addition, we provide initial parameters, eccentricities, radiated linear and angular momentum, precession rates and remnant mass, spin, and recoils for all 48 configurations. Our results indicate that surveys exploring peculiar (redshifted or blueshifted) differential line-of-sight velocities should observe at least one case above 2000 km s^{-1} out of four thousand merged galaxies. On the other hand, the probability that a remnant BH recoils in any direction at a velocity exceeding the $\sim 2000 \text{ km s}^{-1}$ escape velocity of large elliptical galaxies is 0.03%. Probabilities of recoils exceeding the escape velocity quickly rise to 5% for galaxies with escape velocities of 1000 km s^{-1} and nearly 20% for galaxies with escape velocities of 500 km s^{-1} . In addition the direction of these large recoils is strongly peaked toward the angular momentum axis, with very low probabilities of recoils exceeding 350 km s^{-1} for angles larger than 45° with respect to the orbital angular momentum axis.

PACS numbers: 04.25.dg, 04.30.Db, 04.25.Nx, 04.70.Bw

I. INTRODUCTION

Speculations about the relevance of gravitational recoils in astrophysical black-hole binary (BHB) mergers can be traced back at least thirty years [1, 2]. The crucial scale of the problem is when those recoils reach velocities comparable to the escape velocities of the relevant structures, i.e. globular clusters, which have escape velocities of 10s of km s^{-1} , and dwarf, spiral, and giant elliptical galaxies, which have escape velocities from 100s to $\sim 1000 \text{ km s}^{-1}$ for normal galaxies. For large galaxies undergoing major mergers the effective escape velocity can be up to a factor of a few higher at the time of coalescence, as the central potential well deepens rapidly at that time. Once the merger is complete and the stellar systems begins to relax, the potential becomes shallower [3].

Early attempts to compute recoil velocities from BHB mergers used perturbative [4, 5] and post-Newtonian approximations (see [6] for a review up to 2005) and found recoils up to a few hundred km s^{-1} , but uncertainties in the computations were of the same order of magnitude as those velocities (see [7] for a more current review). The first computation that used full numerical simulations within the Lazarus approach produced similar results [8].

The accurate computation of recoil velocities had to wait for the 2005 breakthroughs [9–11] in Numerical relativity (NR), since it proved to be a genuinely strong-field, highly nonlinear General Relativistic phenomenon. The first systematic study of recoil velocities considered

unequal mass, nonspinning BHBs [12]. That study found that the maximum recoil velocity for non-spinning BHBs is 175 km s^{-1} , which occurs for a mass ratio near 1:3.

Unexpectedly, spinning BHBs, with individual spins anti-aligned with each other and both parallel to the angular momentum direction were found to produce recoils of over a factor two larger than the unequal-mass maximum [13, 14], and a revolution occurred when it was discovered [15] that a configuration of the spins lying in the orbital plane led to recoils of almost [16, 17] 4000 km s^{-1} . This last figure caught the attention of observational astronomers who began to look for these highly-recoiling BHs by searching the spectral data of galaxies for differential redshifts of several thousand km s^{-1} . The idea there was that gas close to the BH would remain bound to it, while gas further out in the accretion disk would be left behind. The two gas components would then have different relative redshifts. Initial searches produced the first supermassive recoiling BH candidates [18–21] and now more thorough surveys have increased the numbers of potential candidates to several dozen [22, 23]. These observations may provide the first confirmation of a general relativistic strong field, highly-dynamical, full-numerical prediction.

A recent study [17] pointed out that configurations with partially aligned spins, which we call the “hangup-kick” configuration, can lead to even larger recoil velocities, of nearly 5000 km s^{-1} . More importantly, these configurations are favored with respect to the “spin in the orbital plane” configuration by the effects of accre-

tion on the BHs during very early orbital (Newtonian) stages [24, 25]. We address this question in more detail in this paper.

This paper is organized as follows. In Sec. II we review the numerical methodology to perform the simulations. In Sec. III, we describe the initial configurations of a family of BHBs chosen to model “hangup-kicks”. In Sec. IV, we provide the main results of these evolutions in tables of radiated energies, angular and linear momenta, as well as final remnant mass and spin. We then model recoils using empirical fitting formulas. In Sec. V we describe smoothed particle hydrodynamics (SPH) simulations that model accretion onto BHBs to obtain the spin magnitude and direction distribution of the individual spins in merging BHBs for our full numerical simulations. Using these spin direction and magnitude distributions, we give predictions for the recoil distribution and the probabilities of observing large recoils. We discuss the consequences and future extensions of these techniques in Sec. VIII.

II. NUMERICAL RELATIVITY TECHNIQUES

We use the TwoPunctures thorn [26] to generate initial puncture data [27] for the black-hole binary (BHB) simulations described below. These data are characterized by mass parameters m_p , which are not the horizon masses, of each BH, as well as the momentum and spin of each BH. We evolve these BHB data-sets using the LAZEV [28] implementation of the moving puncture approach [10, 11] with the conformal function $W = \sqrt{\chi} = \exp(-2\phi)$ suggested by Ref. [29]. For the runs presented here, we use centered, eighth-order finite differencing in space [30] and a fourth-order Runge Kutta time integrator. (Note that we do not upwind the advection terms.)

Our code uses the CACTUS/EINSTEINTOOLKIT [31, 32] infrastructure. We use the CARPET [33] mesh refinement driver to provide a “moving boxes” style of mesh refinement. In this approach refined grids of fixed size are arranged about the coordinate centers of both holes. The CARPET code then moves these fine grids about the computational domain by following the trajectories of the two BHs.

We obtain accurate, convergent waveforms and horizon parameters by evolving this system in conjunction with a modified 1+log lapse and a modified Gamma-driver shift condition [10, 34, 35], and an initial lapse $\alpha(t=0) = 2/(1 + \psi_{BL}^4)$, where ψ_{BL} is the Brill-Lindquist conformal factor and is given by

$$\psi_{BL} = 1 + \sum_{i=1}^n m_i^p / (2|\vec{r} - \vec{r}_i|),$$

where \vec{r}_i is the coordinate location of puncture i . The lapse and shift are evolved with

$$(\partial_t - \beta^i \partial_i)\alpha = -2\alpha K, \quad (1a)$$

$$\partial_t \beta^a = (3/4)\tilde{\Gamma}^a - \eta \beta^a, \quad (1b)$$

where we use $\eta = 2$ for all simulations presented below.

We use AHFINDERDIRECT [36] to locate apparent horizons. We measure the magnitude of the horizon spin using the Isolated Horizon algorithm detailed in Ref. [37]. Note that once we have the horizon spin, we can calculate the horizon mass via the Christodoulou formula

$$m_H = \sqrt{m_{\text{irr}}^2 + S_H^2 / (4m_{\text{irr}}^2)}, \quad (2)$$

where $m_{\text{irr}} = \sqrt{A/(16\pi)}$ and A is the surface area of the horizon, and S_H is the spin angular momentum of the BH (in units of M^2). In the tables below, we use the variation in the measured horizon irreducible mass and spin during the simulation as a measure of the error in these quantities. We measure radiated energy, linear momentum, and angular momentum, in terms of the radiative Weyl Scalar ψ_4 , using the formulas provided in Refs. [38, 39]. However, rather than using the full ψ_4 , we decompose it into ℓ and m modes and solve for the radiated linear momentum, dropping terms with $\ell \geq 5$. The formulas in Refs. [38, 39] are valid at $r = \infty$. We extract the radiated energy-momentum at finite radius and extrapolate to $r = \infty$ using both linear and quadratic extrapolations. We use the difference of these two extrapolations as a measure of the error.

III. SIMULATIONS

We evolved a set of 48 equal-mass, spinning, quasi-circular, “hangup-kick” configurations, with 30 simulations having individual BH spins of magnitude $\alpha = 1/\sqrt{2}$ and 18 simulations having BH spin magnitudes of $\alpha = 0.9$, where $\vec{\alpha}$ is the dimensionless spin of the BH ($\vec{\alpha} = \vec{S}_H/M_H^2$, where \vec{S}_H is the spin angular momentum and M_H is the mass of the BH). In the “hangup-kick” configuration, the z components of the individual spins are equal, while the projections of the individual spins onto the orbital plane are equal in magnitude but opposite in direction. The $\alpha = 1/\sqrt{2}$ configurations were split into five sets of 6, where the runs in each individual set had the same initial angle θ between the spin direction and orbital angular momentum direction (here we chose $\theta = 22.5^\circ, 45^\circ, 60^\circ, 120^\circ, 135^\circ$). In each set with a given θ , we chose the initial orientation ϕ_i between the in-plane spin and linear momentum to be $0^\circ, 30^\circ, 90^\circ, 130^\circ, 210^\circ$, and 315° . For the $\alpha = 0.9$ runs, we used the same initial 6 ϕ_i configurations for $\theta = 60^\circ, \theta = 30^\circ$, and $\theta = 15^\circ$. We combine these results with the simulations of [40] (which have $\theta = 90^\circ$) in order to perform our analysis below.

Initial data parameters for the 48 simulations are given in Table I. We denote these configurations by AsTHxxxPHYyy, where s indicates the approximate individual spin magnitude (7 for $\alpha_i = 1/\sqrt{2}$ and 9 for $\alpha_i = 0.9$), xxx indicates the angle the spin makes with respect to the z axis, and yyy indicates the angle the spin makes with respect to the y axis. Here xxx and yyy

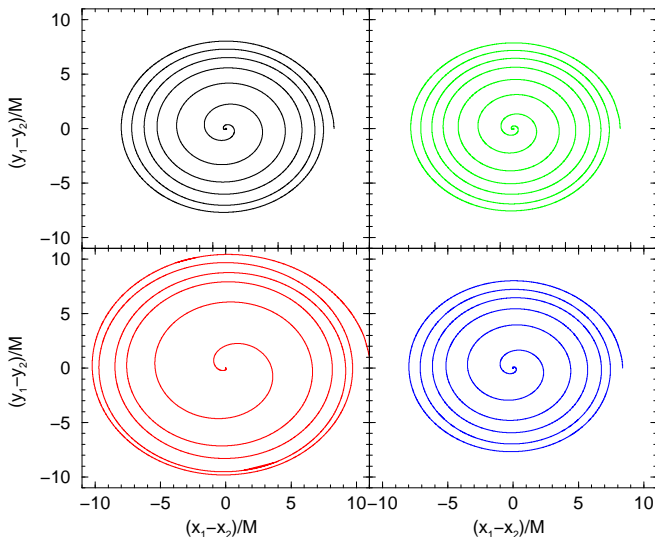


FIG. 1: xy plane projections of the trajectories for various “hangup-kick” configurations. (Top Left) Trajectory for the A7TH22.5PH0 configuration, (Bottom Left) trajectory for the A7TH135PH0 configuration, (Top Right) trajectory for the A9TH15PH0 configuration, (Bottom Right) trajectory for the A9TH60PH0 configuration. The plot shows the trajectories for configurations with the largest and smallest inclination angle for the $\alpha = 1/\sqrt{2}$ and $\alpha = 0.9$ configurations. Note that the eccentricity is larger for large θ and that the eccentricity decreases more slowly.

The orbital motion of these BHBs has an interesting property, the spin precession frequency and the orbital frequency agree right near merger (in these coordinates). Initially the spin precession frequencies are much lower than the orbital frequency, but ramp up dramatically near merger. Figure 3 shows this behavior for the different θ and α configurations (for clarity in the plot, we only show the $\phi_i = 0$ configurations). Interestingly, the strongest effect seems to be due to the inclination angle θ (which is measured with respect to the orbital angular momentum axis, i.e. the z axis) rather than on the projected z spin or total spin. For a given α and θ there are variations with ϕ_i , but these are smaller than the variations with θ . This rapid increase of the precession frequency near merger (as measured with the techniques of [43]), increasing all the way up to the orbital frequency, is in contrast with the much milder increase in the spin magnitude due to weak tidal effects[44]. It also lends support to modeling of black hole merger assuming geodesic precession [45].

In Table II we compare the radiated mass and angular momentum as calculated directly from ψ_4 to the corresponding quantities derived from the remnant mass and spin. The difference between these quantities is a better measurement of the error than those derived from variations in the final horizon mass and spin or in ex-

are in degrees. An eccentricity reduction procedure like those given in [41, 42] could be used to generate configurations with very low eccentricity, but the amount of time required to reduce the eccentricity for 48 configurations would have been too long. We therefore chose to start from 3.5 Post-Newtonian (PN) quasicircular orbital parameters from further separations, such that each binary completed 5-6 orbits prior to merger, and then relied on the radiation of angular momentum during this 5-6 orbit inspiral to reduce the eccentricity. The initial separations varied between $10.16M$ and $8.2M$, depending on the magnitude of the hangup effect, with smaller initial separations for configurations that exhibit larger hangups. Example trajectories for several of these configurations are given in Figs. 1 and 2.

trapolation of the waveform to infinity. That is, there are systematic errors due to truncation error and finite extraction radius, and the difference between these two measurements gives a lower bound to the error.

The dimensionless spin α_{merger} , the orientation φ of the spin during the final orbit and plunge, as well as the remnant BH properties, including recoil velocity, are given in Table III. Note here that the orientation φ is the angle that the spin of BH1 (the BH originally located on the positive x axis) makes with the spin of BH1 in the corresponding A θ TH α PH0 configuration in a rotated frame where infall directions all coincide (see [46]). Also note that the largest measured recoil for these runs is $(4079.5 \pm 10.1) \text{ km s}^{-1}$ for the A9TH60PH30 and A9TH60PH210 configurations, which exceeds both the largest measured quasicircular “superkick recoil” of 3300 km s^{-1} [47] and even the theoretical “superkick maximum” recoil of $3680 \pm 130 \text{ km s}^{-1}$ [40]. The values given for the spins near merger should only be taken as an approximation. The spin-up apparent in the A9TH60 simulations (i.e. the difference between α_{merger} and the initial spin of $\alpha = 0.9$) was due to the lower resolution used in these simulations (simulations of A9TH45 with the same resolution as A9TH60 showed an even stronger spin-up at late times that converged away with higher resolution). Interestingly, these highly-spinning configu-

TABLE I: Initial data parameters for the 48 ‘‘hangup-kick’’ configurations. In all cases the puncture masses were chosen such that the total ADM mass of the binary was $1.0 \pm 10^{-6}M$. Here the punctures are located at $\pm(x, 0, 0)$ with momenta $\pm(0, p, 0)$ and spins $\vec{S} = (\pm S_x, \pm S_y, S_z)$. The approximate initial eccentricities, eccentricities measured over the last orbit, and the number of orbits, are also given.

CONF	m_p/M	x/M	p/M	S_x/M^2	S_y/M^2	S_z/M^2	$(e_{\text{init}}, N_{\text{orbits}}, e_{\text{merge}})$
A7TH22.5PH0	0.361001	4.141042	0.105976	0.000000	0.069426	0.167609	(0.02, 5.5, 0.004)
A7TH22.5PH30	0.361022	4.141042	0.105976	-0.034713	0.060125	0.167609	
A7TH22.5PH90	0.361085	4.141042	0.105976	-0.069426	0.000000	0.167609	
A7TH22.5PH130	0.361050	4.141042	0.105976	-0.053183	-0.044626	0.167609	
A7TH22.5PH210	0.361022	4.141042	0.105976	0.034713	-0.060125	0.167609	
A7TH22.5PH315	0.361043	4.141042	0.105976	0.049092	0.049092	0.167609	
A7TH45PH0	0.360775	4.175510	0.106744	0.000000	0.128222	0.128222	(0.027, 5, 0.0054)
A7TH45PH30	0.360849	4.175510	0.106744	-0.064111	0.111043	0.128222	
A7TH45PH90	0.361068	4.175510	0.106744	-0.128222	0.000000	0.128222	
A7TH45PH130	0.360947	4.175510	0.106744	-0.098224	-0.082419	0.128222	
A7TH45PH210	0.360849	4.175510	0.106744	0.064111	-0.111043	0.128222	
A7TH45PH315	0.360922	4.175510	0.106744	0.090667	0.090667	0.128222	
A7TH60PH0	0.360607	4.207527	0.107470	0.000000	0.156971	0.090627	(0.022, 4.5, 0.0052)
A7TH60PH30	0.360718	4.207527	0.107470	-0.078485	0.135941	0.090627	
A7TH60PH90	0.361052	4.207527	0.107470	-0.156971	0.000000	0.090627	
A7TH60PH130	0.360868	4.207527	0.107470	-0.120246	-0.100899	0.090627	
A7TH60PH210	0.360718	4.207527	0.107470	0.078485	-0.135941	0.090627	
A7TH60PH315	0.360830	4.207527	0.107470	0.110995	0.110995	0.090627	
A7TH120PH0	0.362448	5.295630	0.095864	0.000000	0.156161	-0.090160	(0.026, 5, 0.003)
A7TH120PH30	0.362537	5.295630	0.095864	-0.078081	0.135240	-0.090160	
A7TH120PH90	0.362803	5.295630	0.095864	-0.156161	0.000000	-0.090160	
A7TH120PH130	0.362656	5.295630	0.095864	-0.119627	-0.100379	-0.090160	
A7TH120PH210	0.362537	5.295630	0.095864	0.078081	-0.135240	-0.090160	
A7TH120PH315	0.362625	5.295630	0.095864	0.110423	0.110423	-0.090160	
A7TH135PH0	0.362878	5.534525	0.093655	0.000000	0.127399	-0.127399	(0.02, 5, 0.005)
A7TH135PH30	0.362934	5.534525	0.093655	-0.063699	0.110331	-0.127399	
A7TH135PH90	0.363104	5.534525	0.093655	-0.127399	0.000000	-0.127399	
A7TH135PH130	0.363011	5.534525	0.093655	-0.097593	-0.081890	-0.127399	
A7TH135PH210	0.362934	5.534525	0.093655	0.063699	-0.110331	-0.127399	
A7TH135PH315	0.362991	5.534525	0.093655	0.090085	0.090085	-0.127399	
A9TH15PH0	0.177282	4.094887	0.104887	0.000000	0.059803	0.223187	(0.027, 6, 0.003)
A9TH15PH30	0.177339	4.094887	0.104887	-0.029901	0.051791	0.223187	
A9TH15PH90	0.177509	4.094887	0.104887	-0.059803	0.000000	0.223187	
A9TH15PH130	0.177415	4.094887	0.104887	-0.045811	-0.038440	0.223187	
A9TH15PH210	0.177339	4.094887	0.104887	0.029901	-0.051791	0.223187	
A9TH15PH315	0.177395	4.094887	0.104887	0.042287	0.042287	0.223187	
A9TH30PH0	0.176649	4.116022	0.105345	0.000000	0.115496	0.200045	(0.027, 5.5, 0.003)
A9TH30PH30	0.176864	4.116022	0.105345	-0.057748	0.100022	0.200045	
A9TH30PH90	0.177505	4.116022	0.105345	-0.115496	0.000000	0.200045	
A9TH30PH130	0.177152	4.116022	0.105345	-0.088475	-0.074239	0.200045	
A9TH30PH210	0.176864	4.116022	0.105345	0.057748	-0.100022	0.200045	
A9TH30PH315	0.177078	4.116022	0.105345	0.081668	0.081668	0.200045	
A9TH60PH0	0.174838	4.190252	0.107000	0.000000	0.199841	0.115378	(0.027, 5, 0.0055)
A9TH60PH30	0.175510	4.190252	0.107000	-0.099920	0.173067	0.115378	
A9TH60PH90	0.177498	4.190252	0.107000	-0.199841	0.000000	0.115378	
A9TH60PH130	0.176408	4.190252	0.107000	-0.153087	-0.128455	0.115378	
A9TH60PH210	0.175510	4.190252	0.107000	0.099920	-0.173067	0.115378	
A9TH60PH315	0.176177	4.190252	0.107000	0.141309	0.141309	0.115378	

rations can exhibit both spin-up and spin-down, depending on the location of the refinement boundaries, when not fully resolved. The other A9 runs used higher resolution and show much better spin conservation.

We evolve the A9TH15 and A9TH30 configurations with 10 levels of refinement and maximum resolution of

$h = M/153.6$. The width of this level was $2 \times 0.35M$, while the radius of the horizons grew to $0.24M$. Our initial explorations used grids that were smaller in radius, but we found that using larger grids improved the spin conservation considerably. The A9TH60 configuration were evolved with grids a factor of 1.2 coarser, and

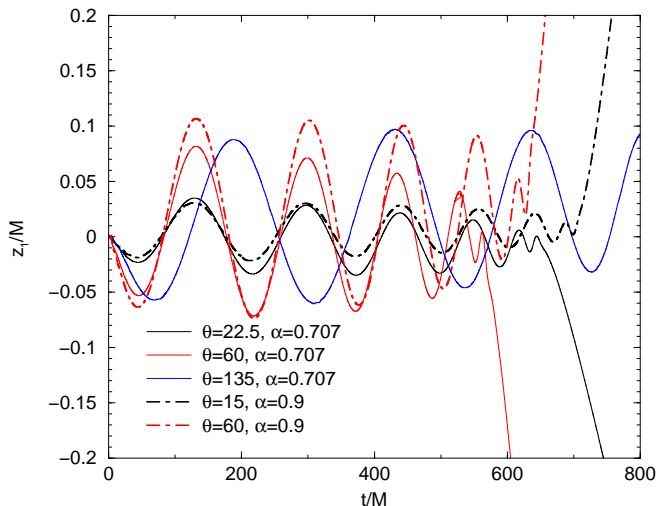


FIG. 2: The elevation of the trajectory as a function of time for the several of the “hangup-kick” configurations. Note that the “bobbing” amplitude does not necessarily correspond to a large recoil. The A7TH135PH0 configuration has a factor of 2 smaller recoil than the A7TH60PH0 configuration, but a slightly larger bobbing amplitude.

IV. RESULTS AND MODELING OF RECOIL VELOCITIES

With the discovery of very large recoil [15] velocities for certain configurations of merging spinning BHBs, the need for an empirical model for the recoil velocity as a function of the progenitor’s parameters was apparent. Our approach to provide that phenomenological formula was based on the observation that the recoil of spinning BHs is largely generated around the time of merger of the two holes [48]; and that this nearly instantaneous burst of radiation of linear momentum can be modeled by a parametrized dependence of the leading (on spins and mass ratio) post-Newtonian (PN) expressions for the linear momentum radiated[49].

In Ref. [50] we extended our original empirical formula for the recoil velocity imparted to the remnant of a BHB merger [15, 16] to include next-to-leading-order corrections (based on the PN work of [51]), still linear in the spins

$$\vec{v}_{\text{recoil}}(q, \vec{\alpha}) = v_m \hat{e}_1 + v_{\perp} (\cos \xi \hat{e}_1 + \sin \xi \hat{e}_2) + v_{\parallel} \hat{n}_{\parallel}, \quad (3)$$

consequently the spins near merger are not as accurate. Note that these A9TH60 runs were performed first, and based on the errors in these simulations, we refined the grid for the other A9 runs.

where

$$\begin{aligned} v_m &= A_m \frac{\eta^2(1-q)}{(1+q)} [1 + B_m \eta], \\ v_{\perp} &= H \frac{\eta^2}{(1+q)} \left[(1 + B_H \eta) (\alpha_2^{\parallel} - q\alpha_1^{\parallel}) \right. \\ &\quad \left. + H_S \frac{(1-q)}{(1+q)^2} (\alpha_2^{\parallel} + q^2\alpha_1^{\parallel}) \right], \\ v_{\parallel} &= K \frac{\eta^2}{(1+q)} \left[(1 + B_K \eta) |\bar{\alpha}_2^{\perp} - q\bar{\alpha}_1^{\perp}| \right. \\ &\quad \times \cos(\phi_{\Delta} - \phi_1) \\ &\quad \left. + K_S \frac{(1-q)}{(1+q)^2} |\bar{\alpha}_2^{\perp} + q^2\bar{\alpha}_1^{\perp}| \right. \\ &\quad \left. \times \cos(\phi_S - \phi_2) \right], \end{aligned} \quad (4)$$

and $\eta = q/(1+q)^2$, with $q = m_1/m_2$ the mass ratio of the smaller to larger mass hole, $\bar{\alpha}_i = \vec{S}_i/m_i^2$, m_i is shorthand for m_{H_i} the mass of BH i , the index \perp and \parallel refer to perpendicular and parallel to the orbital angular momentum respectively, \hat{e}_1, \hat{e}_2 are orthogonal unit vectors in the orbital plane, and ξ measures the angle between the unequal mass and spin contribution to the recoil velocity in the orbital plane. The angles ϕ_{Δ} and ϕ_S are defined as the angle between the in-plane component $\vec{\Delta}^{\perp} = M(\vec{S}_2^{\perp}/m_2 - \vec{S}_1^{\perp}/m_1)$ and $\vec{S}^{\perp} = \vec{S}_1^{\perp} + \vec{S}_2^{\perp}$ respectively and a fiducial direction at merger (see Ref. [46] for a description of the technique).

TABLE II: A comparison of the radiated mass and angular momentum with the predictions based on the final remnant mass and spin and the initial ADM mass and angular momentum for the 48 “hang-up-kick” configurations.

CONF	$(M_{\text{ADM}} - M_H)/M$	$\delta E_{\text{rad}}/M$	$(J_{\text{ADM}}^z - S_H^z)/M^2$	$\delta J_{\text{rad}}^z/M^2$
A7TH22.5PH0	0.065949 ± 0.000113	0.063479 ± 0.000169	0.452347 ± 0.001590	0.440182 ± 0.006183
A7TH22.5PH30	0.065440 ± 0.000125	0.063034 ± 0.000164	0.450602 ± 0.001706	0.438756 ± 0.006006
A7TH22.5PH90	0.065188 ± 0.000121	0.062822 ± 0.000171	0.450332 ± 0.001675	0.439398 ± 0.005161
A7TH22.5PH130	0.065842 ± 0.000105	0.063363 ± 0.000190	0.452581 ± 0.001493	0.440443 ± 0.005901
A7TH22.5PH210	0.065440 ± 0.000125	0.063035 ± 0.000165	0.450601 ± 0.001706	0.438766 ± 0.005996
A7TH22.5PH315	0.065910 ± 0.000105	0.063423 ± 0.000188	0.452761 ± 0.001487	0.440460 ± 0.006077
A7TH45PH0	0.058764 ± 0.000006	0.056538 ± 0.000181	0.417697 ± 0.000084	0.403669 ± 0.007395
A7TH45PH30	0.058594 ± 0.000008	0.056460 ± 0.000153	0.416460 ± 0.000088	0.403290 ± 0.006741
A7TH45PH90	0.056266 ± 0.000010	0.054394 ± 0.000120	0.408936 ± 0.000072	0.397875 ± 0.004794
A7TH45PH130	0.056959 ± 0.000010	0.054940 ± 0.000155	0.412016 ± 0.000078	0.399658 ± 0.005982
A7TH45PH210	0.058594 ± 0.000008	0.056460 ± 0.000153	0.416459 ± 0.000088	0.403290 ± 0.006739
A7TH45PH315	0.057167 ± 0.000008	0.055120 ± 0.000159	0.412756 ± 0.000078	0.400125 ± 0.006224
A7TH60PH0	0.050887 ± 0.000004	0.049046 ± 0.000145	0.379033 ± 0.000032	0.365962 ± 0.007685
A7TH60PH30	0.052125 ± 0.000003	0.050267 ± 0.000146	0.383455 ± 0.000029	0.371173 ± 0.006948
A7TH60PH90	0.051234 ± 0.000005	0.049628 ± 0.000094	0.378829 ± 0.000027	0.368250 ± 0.005342
A7TH60PH130	0.049522 ± 0.000004	0.047918 ± 0.000103	0.372896 ± 0.000025	0.361386 ± 0.006580
A7TH60PH210	0.052124 ± 0.000003	0.050266 ± 0.000146	0.383456 ± 0.000029	0.371168 ± 0.006945
A7TH60PH315	0.049445 ± 0.000004	0.047811 ± 0.000112	0.372866 ± 0.000030	0.360951 ± 0.006697
A7TH120PH0	0.033193 ± 0.000002	0.032297 ± 0.000048	0.303865 ± 0.000005	0.298884 ± 0.006258
A7TH120PH30	0.033107 ± 0.000002	0.032297 ± 0.000010	0.303095 ± 0.000005	0.295666 ± 0.008881
A7TH120PH90	0.031686 ± 0.000002	0.031037 ± 0.000015	0.297018 ± 0.000005	0.292110 ± 0.006177
A7TH120PH130	0.031974 ± 0.000002	0.031188 ± 0.000044	0.298771 ± 0.000005	0.297030 ± 0.002584
A7TH120PH210	0.033107 ± 0.000002	0.032298 ± 0.000010	0.303097 ± 0.000005	0.295663 ± 0.008889
A7TH120PH315	0.032117 ± 0.000002	0.031308 ± 0.000051	0.299419 ± 0.000005	0.297731 ± 0.002485
A7TH135PH0	0.029675 ± 0.000004	0.029004 ± 0.000024	0.287481 ± 0.000006	0.290758 ± 0.000188
A7TH135PH30	0.030091 ± 0.000004	0.029449 ± 0.000043	0.289543 ± 0.000005	0.293205 ± 0.000038
A7TH135PH90	0.030000 ± 0.000004	0.029437 ± 0.000063	0.288696 ± 0.000006	0.294013 ± 0.001881
A7TH135PH130	0.029415 ± 0.000003	0.028803 ± 0.000032	0.285893 ± 0.000006	0.290818 ± 0.001668
A7TH135PH210	0.030085 ± 0.000004	0.029448 ± 0.000048	0.289513 ± 0.000006	0.293050 ± 0.000149
A7TH135PH315	0.029385 ± 0.000004	0.028766 ± 0.000032	0.285792 ± 0.000006	0.290244 ± 0.001187
A9TH15PH0	0.086926 ± 0.000422	0.082160 ± 0.000612	0.540966 ± 0.004231	0.523516 ± 0.003980
A9TH15PH30	0.087312 ± 0.000396	0.082564 ± 0.000612	0.541701 ± 0.003972	0.524385 ± 0.004228
A9TH15PH90	0.086773 ± 0.000341	0.082188 ± 0.000602	0.539095 ± 0.003287	0.523929 ± 0.003074
A9TH15PH130	0.086317 ± 0.000384	0.081695 ± 0.000599	0.538447 ± 0.003722	0.522743 ± 0.002983
A9TH15PH210	0.087315 ± 0.000394	0.082564 ± 0.000612	0.541724 ± 0.003950	0.524384 ± 0.004228
A9TH15PH315	0.086325 ± 0.000394	0.081686 ± 0.000600	0.538588 ± 0.003835	0.522588 ± 0.003187
A9TH30PH0	0.077615 ± 0.000339	0.073045 ± 0.000461	0.509243 ± 0.005934	0.484306 ± 0.004248
A9TH30PH30	0.076957 ± 0.000316	0.072527 ± 0.000493	0.507180 ± 0.005340	0.483676 ± 0.004906
A9TH30PH90	0.078900 ± 0.000166	0.074900 ± 0.000485	0.510059 ± 0.002727	0.496097 ± 0.000678
A9TH30PH130	0.079891 ± 0.000209	0.075617 ± 0.000486	0.513344 ± 0.003666	0.496170 ± 0.000939
A9TH30PH210	0.076956 ± 0.000316	0.072556 ± 0.000469	0.507180 ± 0.005341	0.483678 ± 0.004902
A9TH30PH315	0.079810 ± 0.000224	0.075477 ± 0.000486	0.513380 ± 0.003973	0.495112 ± 0.001297
A9TH60PH0	0.056289 ± 0.000311	0.055634 ± 0.000322	0.387215 ± 0.007605	0.411510 ± 0.009728
A9TH60PH30	0.059774 ± 0.000325	0.058422 ± 0.000326	0.402796 ± 0.005399	0.422236 ± 0.007268
A9TH60PH90	0.054809 ± 0.000087	0.052769 ± 0.000184	0.394238 ± 0.001762	0.396247 ± 0.003734
A9TH60PH130	0.055249 ± 0.000168	0.053567 ± 0.000241	0.392036 ± 0.003341	0.399533 ± 0.008047
A9TH60PH210	0.059774 ± 0.000325	0.058422 ± 0.000326	0.402796 ± 0.005399	0.422236 ± 0.007268
A9TH60PH315	0.054902 ± 0.000201	0.053558 ± 0.000260	0.388072 ± 0.004485	0.400454 ± 0.008515

Note that $\vec{\Delta} = M(\vec{S}_2/m_2 - \vec{S}_1/m_1)$ can be expressed as $\vec{\Delta} = M^2(\vec{\alpha}_2 - q\vec{\alpha}_1)/(1+q)$. Phases ϕ_1 and ϕ_2 depend on the initial separation of the holes for quasicircular orbits (astrophysically realistic evolutions of comparable masses BHs lead to nearly zero eccentricity mergers).

The most recent published estimates for the above parameters can be found in [46, 52] and references therein.

The current best estimates are: $A_m = 1.2 \times 10^4 \text{ km s}^{-1}$, $B_m = -0.93$, $H = (6.9 \pm 0.5) \times 10^3 \text{ km s}^{-1}$, $K = (5.9 \pm 0.1) \times 10^4 \text{ km s}^{-1}$, and $\xi \sim 145^\circ$, and $K_S = -4.254$. Here we set B_H and B_K to zero, which is consistent with the findings in [50], where it was found that the uncertainties in the coefficients are of the same magnitude as the coefficients themselves.

Although the post-Newtonian approximation fails to

TABLE III: Merger and remnant BH properties of the 48 configurations. S_H is the spin angular momentum of the remnant, M_H is the Christodoulou mass, V_{recoil}^z is the recoil velocity, α_{merger} is an approximate value of the dimensionless spin during the merger phase, and φ is the angle between the direction of the spin of BH1 (in the rotated frame) and the spin of BH1 in the corresponding PH0 configuration (see Section IV).

CONF	M_H/M	S_H/M^2	V_{recoil}^z (km s $^{-1}$)	α_{merger}	φ
A7TH22.5PH0	0.934051 \pm 0.000113	0.760575 \pm 0.001590	-925.3 \pm 1.0	0.71	0
A7TH22.5PH30	0.934560 \pm 0.000125	0.762320 \pm 0.001706	-7.9 \pm 2.3	0.71	31.53
A7TH22.5PH90	0.934812 \pm 0.000121	0.762590 \pm 0.001675	1531.5 \pm 2.6	0.71	91.68
A7TH22.5PH130	0.934158 \pm 0.000105	0.760341 \pm 0.001493	1735.2 \pm 1.2	0.71	131.14
A7TH22.5PH210	0.934560 \pm 0.000125	0.762321 \pm 0.001706	8.0 \pm 2.3	0.71	211.52
A7TH22.5PH315	0.934089 \pm 0.000105	0.760161 \pm 0.001487	-1703.7 \pm 1.1	0.71	315.97
A7TH45PH0	0.941235 \pm 0.000006	0.730165 \pm 0.000084	2527.7 \pm 5.4	0.71	0
A7TH45PH30	0.941406 \pm 0.000008	0.731403 \pm 0.000088	1708.6 \pm 1.2	0.71	29.33
A7TH45PH90	0.943734 \pm 0.000010	0.738926 \pm 0.000072	-1199.6 \pm 4.8	0.71	91.22
A7TH45PH130	0.943041 \pm 0.000010	0.735846 \pm 0.000078	-2486.4 \pm 0.2	0.71	131.57
A7TH45PH210	0.941406 \pm 0.000008	0.731403 \pm 0.000088	-1708.2 \pm 1.3	0.71	209.35
A7TH45PH315	0.942833 \pm 0.000008	0.735106 \pm 0.000078	2569.6 \pm 0.7	0.71	316.39
A7TH60PH0	0.949113 \pm 0.000004	0.706585 \pm 0.000032	-2786.0 \pm 4.6	0.71	0
A7TH60PH30	0.947875 \pm 0.000003	0.702163 \pm 0.000029	-2886.8 \pm 2.9	0.71	27.78
A7TH60PH90	0.948766 \pm 0.000005	0.706789 \pm 0.000027	-968.8 \pm 0.4	0.71	89.42
A7TH60PH130	0.950477 \pm 0.000004	0.712722 \pm 0.000025	1167.1 \pm 4.6	0.71	129.89
A7TH60PH210	0.947876 \pm 0.000003	0.702162 \pm 0.000029	2886.7 \pm 3.0	0.71	207.73
A7TH60PH315	0.950555 \pm 0.000004	0.712752 \pm 0.000030	-1495.7 \pm 5.5	0.71	316.71
A7TH120PH0	0.966806 \pm 0.000002	0.531135 \pm 0.000005	1754.0 \pm 6.7	0.71	0
A7TH120PH30	0.966893 \pm 0.000002	0.531905 \pm 0.000005	1370.2 \pm 5.4	0.71	29.99
A7TH120PH90	0.968314 \pm 0.000002	0.537982 \pm 0.000005	-269.0 \pm 1.3	0.71	86.11
7TH120PH130	0.968026 \pm 0.000002	0.536229 \pm 0.000005	-1400.6 \pm 3.5	0.71	129.11
A7TH120PH210	0.966893 \pm 0.000002	0.531903 \pm 0.000005	-1370.7 \pm 5.4	0.71	209.98
A7TH120PH315	0.967883 \pm 0.000002	0.535581 \pm 0.000005	1495.8 \pm 4.1	0.71	314.62
A7TH135PH0	0.970326 \pm 0.000004	0.494390 \pm 0.000006	1108.0 \pm 1.1	0.71	0
A7TH135PH30	0.969909 \pm 0.000004	0.492329 \pm 0.000005	1328.0 \pm 1.9	0.71	28.77
A7TH135PH90	0.970000 \pm 0.000004	0.493176 \pm 0.000006	775.6 \pm 2.0	0.71	90.61
A7TH135PH130	0.970585 \pm 0.000003	0.495978 \pm 0.000006	-207.1 \pm 0.6	0.71	133.14
A7TH135PH210	0.969915 \pm 0.000004	0.492359 \pm 0.000006	-1326.6 \pm 1.9	0.71	208.32
A7TH135PH315	0.970615 \pm 0.000004	0.496080 \pm 0.000006	332.6 \pm 0.4	0.71	318.33
A9TH15PH0	0.913073 \pm 0.000422	0.764409 \pm 0.004231	2028.2 \pm 20.6	0.90	0
A9TH15PH30	0.912688 \pm 0.000396	0.763674 \pm 0.003972	1764.0 \pm 23.2	0.90	30.06
A9TH15PH90	0.913227 \pm 0.000341	0.766280 \pm 0.003287	22.9 \pm 8.4	0.90	91.51
A9TH15PH130	0.913683 \pm 0.000384	0.766929 \pm 0.003722	-1323.0 \pm 9.6	0.90	130.98
A9TH15PH210	0.912685 \pm 0.000394	0.763651 \pm 0.003950	-1763.9 \pm 23.2	0.90	210.02
A9TH15PH315	0.913676 \pm 0.000394	0.766788 \pm 0.003835	1455.4 \pm 11.0	0.90	316.18
A9TH30PH0	0.922385 \pm 0.000339	0.758052 \pm 0.005934	-886.8 \pm 13.6	0.895	0
A9TH30PH30	0.923043 \pm 0.000316	0.760116 \pm 0.005340	-2358.8 \pm 6.0	0.895	28.07
A9TH30PH90	0.921100 \pm 0.000166	0.757236 \pm 0.002727	-3346.5 \pm 34.1	0.895	80.64
A9TH30PH130	0.920108 \pm 0.000209	0.753952 \pm 0.003666	-2306.6 \pm 39.5	0.895	122.75
A9TH30PH210	0.923043 \pm 0.000316	0.760115 \pm 0.005341	2360.4 \pm 4.9	0.895	208.02
A9TH30PH315	0.920190 \pm 0.000224	0.753916 \pm 0.003973	2040.8 \pm 38.7	0.895	308.95
A9TH60PH0	0.943710 \pm 0.000311	0.740252 \pm 0.007605	3792.7 \pm 5.4	0.92	0
A9TH60PH30	0.940226 \pm 0.000325	0.724671 \pm 0.005399	4079.5 \pm 10.1	0.92	36.83
A9TH60PH90	0.945191 \pm 0.000087	0.733228 \pm 0.001762	-2352.1 \pm 1.6	0.92	146.22
A9TH60PH130	0.944751 \pm 0.000168	0.735431 \pm 0.003341	-3054.6 \pm 0.7	0.92	160.22
A9TH60PH210	0.940226 \pm 0.000325	0.724671 \pm 0.005399	-4079.5 \pm 10.1	0.92	216.90
A9TH60PH315	0.945098 \pm 0.000201	0.739395 \pm 0.004485	2772.5 \pm 0.8	0.92	334.02

provide accurate amplitudes for each velocity component, the above parametrization and fitting to a set of full numerical simulations has shown its predictive power in a number of occasions; for instance by predicting the mass ratio dependence that was later confirmed by sets of lengthy numerical simulations[46]. The success of the

original formula allowed the study of higher-order dependencies on the spin of the holes. In a previous study [40], we found that the “superkick” recoil (where the two BHs have equal mass, equal intrinsic spin magnitudes α , and spins lying in the orbital plane in opposite directions) has the following dependence on the intrinsic spin α and

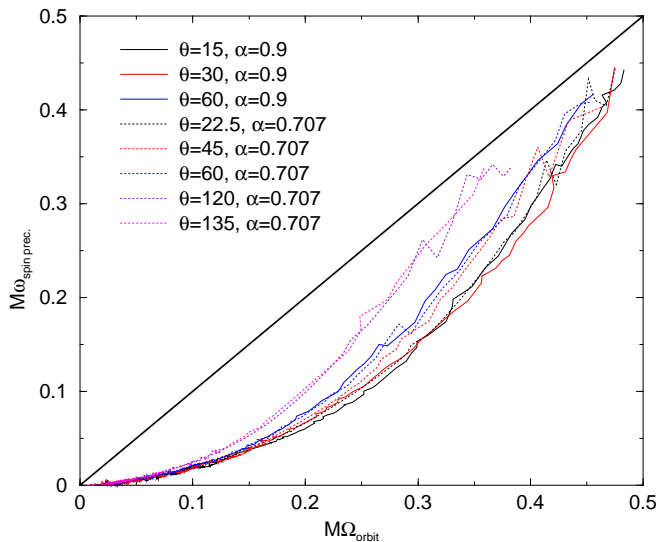


FIG. 3: Spin precession frequency versus orbital frequencies for $\alpha = 1/\sqrt{2}$ and $\alpha = 0.9$ configurations. In each case, only the $\phi_i = 0$ configuration is shown. The trend appears to be (but see $\theta = 30$ for $\alpha = 0.9$) that $\omega_{\text{spin prec.}}$ increases as θ increases, with very little variation with the z component of the spin or even total spin α . Note that at late times (larger Ω_{orbit}) $\omega_{\text{spin prec.}}$ approaches Ω_{orbit} , indicating that the spin processes at nearly the same rate as the orbit during the final orbit and plunge.

orientation ϕ (the angle between the in-plane spin vector and the infall direction near merger),

$$\begin{aligned} V &= V_1 \cos(\phi - \phi_1) + V_3 \cos(3\phi - 3\phi_3), \\ V_1 &= V_{1,1}\alpha + V_{1,3}\alpha^3, \\ V_3 &= V_{3,1}\alpha + V_{3,3}\alpha^3, \end{aligned} \quad (5)$$

where $V_{1,3} = (-15.46 \pm 2.66) \text{ km s}^{-1}$, $V_{3,1} = (15.65 \pm 3.01) \text{ km s}^{-1}$, and $V_{3,3} = (105.90 \pm 4.50) \text{ km s}^{-1}$, while $V_{1,1} = (3681.77 \pm 2.66) \text{ km s}^{-1}$. From that study, it was clear that in the “superkick” configuration, the dominant contribution, even at large α , is linear in α and proportional to $\cos(\phi)$. Note that because of the small contributions of V_3 and $V_{1,3}$, we neglect these terms in the statistical studies below (where we take a uniform distribution in $\phi - \phi_1$).

In Ref. [53] an alternative approach to fitting recoil and remnant mass and spin of a merged BHB was developed. It is based on a Taylor expansion in terms of the binary parameters and exploits all the symmetries of the problem (note that our approach also incorporates these symmetries because it is based on PN formulas for the instantaneous recoil). Using one of our previous set of six “superkick” simulations in [16], the authors in [53] fitted the recoil velocities to terms in $\cos(\phi)$ and $\cos(3\phi)$ to extract the cubic (in spin) dependence of the recoil from a single set of simulations with constant total spin. We also modeled that cubic dependence with more simulations including a range of spin magnitude in [40]. Ref. [53] also

fitted the recoil velocity as a function of the angle θ that the spins make with the orbital angular momentum using the data from a series of runs reported in Ref. [54]. However, those results are inconclusive since they could not model the recoil as a function of ϕ or model the precession of the orbital plane using the data in Ref. [54].

In order to analyze the results of the present simulations, we use the techniques developed in [46]. Briefly, we rotate each configuration such that the trajectories near merger overlap. We then calculate the spins in this rotated frame. The angle φ is then defined to be the angle between the AsTHxxPHyy spin of BH1 (the BH originally located on the positive x axis) and the spin of BH1 in the corresponding AsTHxxPH0 configuration. Note that, for a given family of fixed spin and spin inclination angle θ , the angle φ and ϕ differ by a constant, which can be absorbed in the fitting constants ϕ_1 and ϕ_3 . We then fit the recoil to the form

$$V_{\text{rec}} = V_1 \cos(\varphi - \phi_1) + V_3 \cos(3\varphi - 3\phi_3) \quad (6)$$

for each set of configurations with the same spin and θ , and then fit the dominant V_1 coefficient as a function of φ . Results from these fits are given in Table IV and Figs. 4-6. Note that A9TH60 runs show the largest discrepancies in the fit, consistent with the larger errors in these simulations due to a coarser global resolution (see Sec. III above).

Based on the “superkick” formula (5), we expected that the recoil would have the form

$$V_1 = (V_{1,1} + V_A \alpha \cos \theta + V_B \alpha^2 \cos^2 \theta + V_C \alpha^3 \cos^3 \theta) \times \alpha \sin \theta, \quad (7)$$

where V_1 is the component of the recoil proportional to $\cos \phi$, $V_{1,1}$ arises from the “superkick” formula, and the remaining terms are proportional to linear, quadratic, and higher orders in $S_z/m^2 = \alpha \cos \theta$ (the spin component in the direction of the orbital angular momentum). Here, we do not consider terms higher-order in the in-plane component of $\vec{\Delta} \propto \vec{a}_2 - q\vec{a}_1$ denoted by Δ^\perp ($\Delta^\perp \propto \alpha \sin \theta$ here), where q is the mass ratio, because our previous studies showed that these terms were small at $\theta = 90^\circ$. A fit to this ansatz (7) showed that the truncated series appears to converge very slowly with coefficients $V_{1,1} = (3677.76 \pm 15.17) \text{ km s}^{-1}$, $V_A = (2481.21 \pm 67.09) \text{ km s}^{-1}$, $V_B = (1792.45 \pm 92.98) \text{ km s}^{-1}$, $V_C = (1506.52 \pm 286.61) \text{ km s}^{-1}$ that have relatively large uncertainties. In addition, we propose the modification

$$V_1 = \left(\frac{1 + E\alpha \cos \theta}{1 + F\alpha \cos \theta} \right) D\alpha \sin \theta \quad (8)$$

which can be thought of as a resummation of Eq. (7) with an additional term $E\alpha \cos \theta$, and fit to D , E , F (where we used the prediction of [40] to model the V_1 for $\theta = 90^\circ$) and find $D = (3684.73 \pm 5.67) \text{ km s}^{-1}$, $E = 0.0705 \pm 0.0127$, and $F = -0.6238 \pm 0.0098$. Note that E is approximately 1/10 of F , indicating that coefficients in

TABLE IV: Fits of recoil velocities as a function of φ for each family of configurations with fixed α and θ to the form Eq. (5).

CONF	V_1 (km s $^{-1}$)	V_3 (km s $^{-1}$)	ϕ_1	ϕ_3
A7TH22.5	1764 ± 1	4.6 ± 0.1	58.36 ± 0.01	280 ± 1
A7TH45	2766 ± 1	41.6 ± 0.9	203.55 ± 0.02	83 ± 2
A7TH60	2972 ± 3	54 ± 3	342.25 ± 0.07	141 ± 4
A7TH120	1806 ± 1	27.4 ± 0.1	191.78 ± 0.01	62 ± 1
A7TH135	1352 ± 1	16.6 ± 0.7	145.21 ± 0.04	277 ± 4
A9TH15	2038 ± 2	27 ± 2	178.55 ± 0.09	291 ± 7
A9TH30	3408 ± 2	42 ± 2	284.91 ± 0.03	285 ± 3
A9TH60	4171 ± 14	87 ± 10	158.3 ± 0.7	17 ± 17

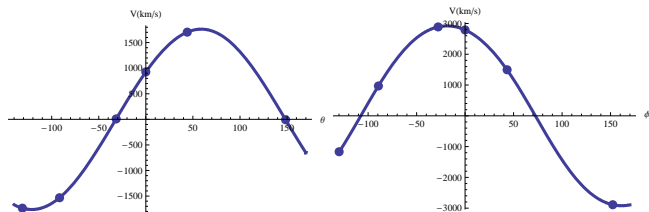


FIG. 4: A fit of V_{recoil} versus φ for the A7TH22.5PHyyy (Left) and A7TH60PHyyy (Right) configurations.

this series get progressively smaller faster than in Eq. (7). Interestingly, a fit to just

$$V_1 = \left(\frac{1}{1 + F\alpha \cos \theta} \right) D\alpha \sin \theta$$

failed to produce sensible results (a badly conditioned matrix was encountered). The two formulas (7) and (8) give very similar results for a broad range of α (see Tables V, VI, and VII). We then use Eq. (8) to predict the recoil for higher spin $\alpha = 0.9$ and test this formula for three angles $\theta = 90^\circ$, $\theta = 60^\circ$, and $\theta = 15^\circ$, with very good agreement (see Fig. 6). In actuality, both Eq. (8) and Eq. (7) provide accurate predictions for our measured recoils at $\alpha = 0.9$. We show the errors in the predictions for the $\alpha = 0.9$ configurations in Table VI.

We also tried fits to

$$V_1 = \left(\frac{1 + E\alpha \cos \theta + G\alpha^2 \cos^2 \theta}{1 + F\alpha \cos \theta} \right) D\alpha \sin \theta, \quad (9)$$

but found that the coefficients were not well determined. In this case, we found $D = 3686.34 \pm 8.87$, $E = 0.055 \pm 0.056$, $F = -0.638 \pm 0.051$, $G = -0.014 \pm 0.050$. The errors in both E and G in this case are larger than the values of the coefficients themselves. We therefore do not use Eq. (9) in the analysis below. Similarly large uncertainties are encountered if the quadratic F correction is in the denominator of Eq. (9) rather than the numerator.

V. BLACK HOLE SPIN EVOLUTION IN GAS RICH GALAXY MERGERS

Full numerical simulations of BHBs typically start when the BHs are at distances of the order of $10M$ from

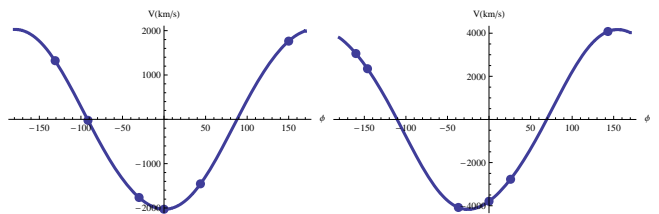


FIG. 5: A fit of V_{recoil} versus φ for the A9TH15PHyyy (Left) and A9TH60PHyyy (Right) configurations.

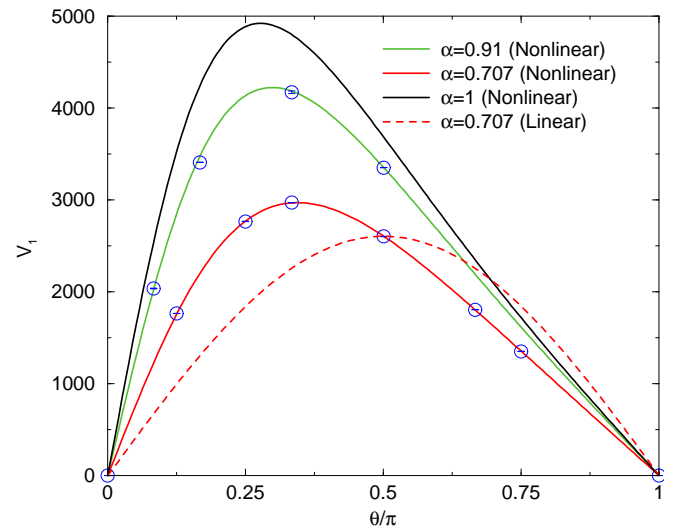


FIG. 6: fit of the recoil (V_1) to the form Eq. (8) for the $\alpha = 1/\sqrt{2}$ configurations, and predictions (based on this fitting) for the $\alpha = 0.91$ recoils. Note how well the $\alpha = 0.91$ curve matches the four measured values. For reference, curves corresponding to the original empirical formula prediction (which only had terms linear in Δ) for $\alpha = 1/\sqrt{2}$ and the new formula for $\alpha = 1$ are also included. Note the skew in the velocity profile compared to the linear predictions.

each other. There are good reasons for this. Numerical runs are still extremely expensive, they need to run on hundreds of nodes for weeks at a time to obtain accurate computations of the gravitational radiation. Those few runs allow us to infer generic behaviors of the remnants, e.g. the modeling of the recoils by the phenomenological Eq. (3). While these initial separations are extremely close by astrophysical standards, most of the nonlinear general relativistic effects take place at these and closer separations. However, if one wants to study statistical distributions of recoils by astrophysical seeds one would like to input realistic spin and mass ratio distributions for the merging BHB. In a first study of such systems we assume an isotropic distribution of the spin direction of the BHs [55]. This could represent “dry” binary mergers. We point out below the relevance of pre-merger accretion to partially align the BH spins with the orbital angular momentum. We then perform a preliminary study of an extended recoil formula (12) to see the differences between the predictions of the recoil formula based on only

TABLE V: Predictions for $\alpha = 1/\sqrt{2}$ simulations based on Eq. (8) (denoted by pade) and Eq. (7) (denoted by FS), as well as the measured V_1 . Note that the $\theta = 90^\circ$ measured value comes from Ref. [40]. Velocities are in units of km s^{-1} .

CONF	$V_{1,\text{pade}}$	$V_{1,\text{FS}}$	$V_{1,\text{meas}}$
TH22.5	1760.46	1754.47	1764
TH45	2771.92	2777.4	2766
TH60	2967.09	2967.33	2972
TH90*	2605.5	2600.57	2603.4
TH120	1802.6	1811.4	1806
TH135	1354.82	1348.48	1352

TABLE VI: Predictions for $\alpha = 0.9$ simulations based on Eq. (8) (denoted by pade) and Eq. (7) (denoted by FS), as well as the measured V_1 . Note that the $\theta = 90^\circ$ measured value comes from Ref. [40]. When applying Eqs. (8) and (7) we use α_{merger} . The relative error quoted here is the relative error in the prediction based on Eq. (8). Velocities are in units of km s^{-1} .

CONF	$V_{1,\text{pade}}$	$V_{1,\text{FS}}$	$V_{1,\text{meas}}$	Rel. Error
TH15	1990	1905.23	2038	-2.4%
TH30	3367	3302.23	3408	-1.2%
TH60	4251	4258.62	4171	1.9%
TH90*	3353.1	3346.76	3350.41	0.1%

linear terms in the spins and the new updated formula [17].

The spins of massive BHs binding in binaries as a result of galaxy mergers can be deeply affected by gas accretion during the last stages of their orbital decay (for separations $\lesssim 100$ pc). This is due to the gas overdensities that the galaxy mergers are expected to convey into the nuclei of the galaxy remnants. Such dense gas structures have a disk like morphology (“circumnuclear disks”), reminiscent of the initial net angular momentum of the inflowing material, as observed in high resolution simulations [e.g. 56, 57] as well as in real merging systems [e.g. 58–60].

Bogdanovic et al [24] proposed a physical process that could *align* the BH spins with the angular momentum of the nuclear disk in which the binary orbit is embedded, thus leading to slow recoils for the BH remnant. The evolution of the spin directions is due to the torques exerted by the gas accreting onto the BHs. Since this process happens on a timescale shorter than the orbital decay of the BHs in the remnant nucleus, the spins tend to align before the two BHs bind in a binary. As a consequence, the evolution of the spin of each BH in this earlier phase can be studied independently, neglecting the presence of the second BH.

The evolution of spin direction and magnitude is governed on small scales (milli-pc, much smaller than the circumnuclear disk within which BHs, and their accretion disks, are embedded). As shown by [61], if the orbital angular momentum of an accretion disk around the BH is misaligned with respect to the BH spin, the coupled

TABLE VII: Angle θ that maximizes the recoil and the maximum recoil as a function of α for Eq. (8) and Eq. (7). Velocities are in units of km s^{-1} while angles are measured in degrees.

α	θ_{pade}	V_{pade} (km s^{-1})	θ_{FS}	V_{FS} (km s^{-1})
0.1	86°	369	86°	369
0.5	70°	1961	70°	1955
0.707	62°	2969	61°	2968
0.91	54°	4225	54°	4232
1	50°	4926	51°	4915

action of viscosity and relativistic Lense-Thirring precession (‘inertial frame dragging’) causes important changes in the structure of an accretion disk, warping the disk. The equilibrium profile of the warped disk can be computed by solving the equation:

$$\frac{1}{R} \frac{\partial}{\partial R} (R \vec{L} v_R) = \frac{1}{R} \frac{\partial}{\partial R} \left(\nu_1 \Sigma R^3 \frac{d\Omega}{dR} \hat{l} \right) + \frac{1}{R} \frac{\partial}{\partial R} \left(\frac{1}{2} \nu_2 R L \frac{\partial \hat{l}}{\partial R} \right) + \frac{2G}{c^2} \frac{\vec{S}_{\text{BH}} \times \vec{L}}{R^3} \quad (10)$$

[see 62], where R is the distance from the BH, v_R is the radial drift velocity, Σ is the surface density, Ω is the Keplerian angular velocity of the gas, and ν_1 (ν_2) is the radial (vertical) viscosity. \vec{L} is the local angular momentum surface density of the disk, defined by its modulus L and the unit vector \hat{l} that defines its direction. The disk profile that is a solution of Eq. (10) is composed of three regions, whose relative importance depends on the values of the specific disk parameters. In the outermost region the angular momentum of the gas is unperturbed by any relativistic effect, and therefore the direction of the disk’s angular momentum is independent of the BH spin. In the inner region, the fluid is forced to rotate in the equatorial plane of the rotating BH, on either prograde or retrograde orbits. Therefore in this inner region the disk is either completely aligned or completely antialigned with respect to the BH spin. Finally, between the inner and outer regions, characterized by different directions of their angular momenta, there exists a transition region, centered at $\sim 100 - 1000$ gravitational radii, where the disk is warped connecting the inner and outer parts of the disk, misaligned one with respect to the other.

The spin of a BH embedded in a warped disk evolves under the influence of the disk itself. The BH spin evolution is described by the equation [62]:

$$\frac{d\vec{S}_{\text{BH}}}{dt} = \dot{M} \Lambda(R_{\text{ISO}}) \hat{l}(R_{\text{ISO}}) + \frac{4\pi G}{c^2} \int_{\text{disk}} \frac{\vec{L} \times \vec{S}_{\text{BH}}}{R^2} dR. \quad (11)$$

The first term in Eq. (11) accounts for the angular momentum deposited onto the BH by the accreted gas at the innermost stable orbit (ISO), where $\Lambda(R_{\text{ISO}})$ denotes the angular momentum per unit mass [Eq. 12.7.18 in 63]

evaluated at R_{ISO} and $\hat{l}(R_{\text{ISO}})$ the local disk angular momentum direction, which is parallel to \vec{S}_{BH} as discussed above. The second term describes the interaction of the BH spin with the warped disk. It is responsible for the evolution of the BH spin direction, and tends to align the direction of the BH spin with the angular momentum of the outer regions of the accretion disk.

The efficiency of the alignment depends on the dynamics of the inflowing material that fuels the small scale accretion disks. It is particularly relevant to determine whether the accretion flow maintains a nearly constant direction of the angular momentum over the growth episode (i.e. the accretion is “coherent”), or not. Only a substantial amount of gas ($1 \sim 10\%$ of the BH mass) accreting from the same plane (for both the BHs) can significantly align the two spins. In order to constrain the degree of coherency of the gas accreting onto the BHs, and to predict the spin configurations in BH binaries, Dotti et al [25] performed numerical simulations of BH pairs in large scale nuclear disks with the N-Body/SPH code GADGET [64], upgraded to include the accretion physics. Here we give a short summary of the initial conditions for the different runs. For a more detailed discussion, we defer the reader to Refs. [25, 65].

The two BHs are placed in the plane of a massive circumnuclear gaseous disk, embedded in a larger stellar spheroid. The disk is modeled with $\approx 2 \times 10^6$ gas particles, has a total mass $M_{\text{Disk}} = 10^8 M_{\odot}$, and follows a Mestel surface density profile $\Sigma(R) \propto R^{-1}$, where R is the radial distance projected into the disk plane. Dotti et al. truncated the disk at an outer radius of 100 pc. The massive disk is rotationally supported in R and has a vertical thickness of 8 pc. Gas is evolved assuming a polytropic equation of state with index $\gamma = 5/3$ or $\gamma = 7/5$. In the former case, the disk is termed “hot” as the temperature is proportional to a higher power of density than in the latter class of models (“cold” cases). The cold case has been shown to provide a good approximation to a gas of solar metallicity heated by a starburst [66, 67]. The hot case instead corresponds to an adiabatic monatomic gas, as if radiative cooling were completely suppressed during the merger, for example as a result of radiative heating after gas accretion onto the BHs [56]. The spheroidal component (bulge) is modeled with 10^5 collisionless particles, initially distributed as a Plummer sphere with a total mass $M_{\text{Bulge}} (= 6.98 \times M_{\text{Disk}})$. The mass of the bulge within 100 pc is five times the mass of the disk, as suggested by [58]. The BHs are equal in mass ($m_{\text{BH}} = 4 \times 10^6 M_{\odot}$), and their initial separation is 50 pc. A BH is placed at rest at the center of the circumnuclear disk, while the other is moving on an initially eccentric ($e_0 \simeq 0.7$) counter-rotating (retrograde BH) or corotating (prograde BH) orbit with respect to the circumnuclear disk. Given the large masses of the disk and the bulge, the dynamics of the moving BH (secondary) is unaffected by the presence of the primary until the BHs form a gravitationally bound system. Furthermore, the gravitational interaction between the orbiting BH and

the rotating gas forces the BH to corotate on almost circular orbits with the disk [68, 69], before the BHs bind in a binary. As a consequence, the initial orbital configurations of the BHs do not influence the final degree of alignment, that, as will be discussed in the following, depends only on the thermodynamical state of the disk.

To follow the evolution of the BH spins, it is necessary to track the dynamics of the gas accreting onto the two central objects. In the simulations discussed in [25] a gas particle can be accreted by a BH if the following two criteria are fulfilled:

- the sum of the kinetic and internal energy of the gas particle is lower than b -times the modulus of its gravitational energy (all the energies are computed with respect to each BH);
- the total mass accreted per unit time onto the BH every timestep is lower than the accretion rate corresponding to the Eddington luminosity computed assuming a radiative efficiency of 10%.

The parameter b is a constant that defines the degree to which a particle is bound to the BH in order to be accreted. Dotti et al [25] set $b = 0.3$. Note that due to the nature of the above criteria, the gas particles can accrete onto the BHs only if the time-varying Bondi-Hoyle-Lyttleton radius is resolved in the simulations. Such a small radius can be resolved only by performing very high resolution simulations. The gravitational softening parameter of the BHs is 0.1 pc. The gravitational softening of the gas particles is set to the same value, in order to prevent numerical errors. This is also the spatial resolution of the hydrodynamical force in the highest density regions[84].

The simulations discussed in Dotti et al [25] cannot follow the dynamics of the accreting gas on unresolved scales. Dotti and collaborators assume that, below the spatial resolution of the runs, gas settles on standard geometrically thin/optically thick α -disks [70]. The properties of those two unresolved disks (one surrounding each of the two BHs of the binary) embedded in the larger scale circumnuclear disk, are determined by the properties of the accreting material. Each gas particle accreted by the BH carries with it mass and angular momentum. These are data Dotti et al. used to model the unresolved accretion discs around the two BHs, becoming the outer boundary conditions for Eq. (10) and (11). Specifically, Dotti and collaborators define \hat{l}_{edge} as the unit vector defining the direction of the angular momentum of the accretion disk in its outermost region, i.e. where it is unaffected by any general relativistic effect. In a warped α -disk the two viscosities (radial, ν_1 and vertical, ν_2) can be described in terms of two different dimensionless viscosity parameters, α_1 and α_2 , through the relations $\nu_{1,2} = \alpha_{1,2} H c_s$, where H is the disk vertical scale height and c_s is the sound speed of the gas in the accretion disk. Additionally, $\alpha_2 = f_2/(2\alpha_1)$, with $\alpha_1 = 0.1$ and $f_2 = 0.6$ [71]. Further details on the procedure used to evolve the BH spins can be found in [62].

The resulting distributions of spin magnitudes and in-

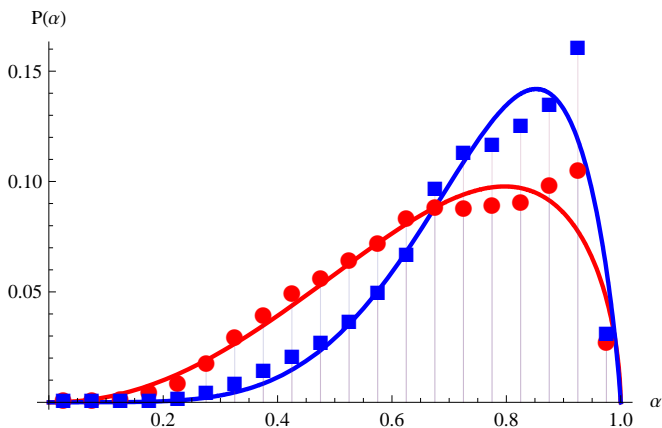


FIG. 7: The probability that the dimensionless spin of a BH in a merging binary has a given magnitude α for BHs in cold disks (squares) and in hot disks (circles). The fits to Beta functions are reasonably good.

clinations with respect to the angular momentum of the newly formed binary are shown in Figs. 7 and 8, respectively. Red circles refer to BHs embedded in hot disks, blue squares to BHs in cold disks. In both the cases, the well defined angular momentum of the large scale nuclear disk results in coherent accretion flows onto the two BHs, and, as a consequence, in high spins strongly aligned with the angular momentum of the BH binary. Note that, in absence of any alignment, the distributions in Fig. 8 should be $\propto \sin(\theta)$ in the whole interval $[0, \pi]$. As discussed in [25], a “hotter” disk, with a stiffer equation of state, is more pressure supported in the center, and, as a consequence, the degree of alignment is lower. Because of this additional support, the accretion rates onto the BHs in the hot runs are lower, corresponding to spin distributions less skewed towards high spin values.

In order to perform the statistical studies below, we fit the spin magnitude and inclination angle distributions above to Beta distributions, which have the form $P(x) \propto (1-x)^{(b-1)}x^{(a-1)}$. Fits to the dimensionless spin magnitudes for BHs in hot and cold gaseous environments give $a = 3.212 \pm 0.258$, $b = 1.563 \pm 0.093$, and $a = 5.935 \pm 0.642$, $b = 1.856 \pm 0.146$, respectively. A comparison of these fits with the measured probabilities of a BH having a given spin magnitude is given in Fig. 7. Fits to the inclination angle for the hot and cold cases angular distributions give $a = 2.018 \pm 0.181$, $b = 5.244 \pm 0.604$, and $a = 2.544 \pm 0.198$, $b = 19.527 \pm 2.075$, respectively. Note that these distributions $P(\theta)$ are for θ in radians. The Beta distribution is not defined for $\theta > 1$, but the data are consistent with near zero probabilities for angles larger than 1 radian. A comparison of these fits with the measured probabilities of a BH having a given spin direction is given in Fig. 8.

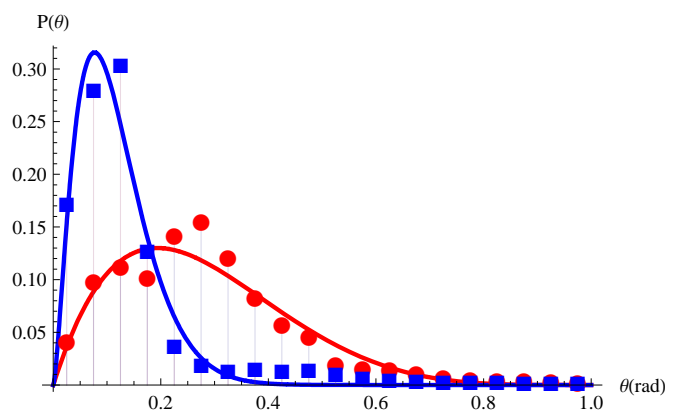


FIG. 8: The probability that the spin of a BH in a merging binary is at an inclination angle θ with respect to the orbital angular momentum for cold (squares) and hot (circles) circumnuclear disks. The fits to Beta functions are reasonably good, but miss the small tail in the cold distribution.

VI. EXTENDING THE HANGUP-KICK FORMULA

While accretion will tend to align the spins of the two BHs in a BHB with the orbital angular momentum, it will not align the in-plane components of the spins. Additionally, the expected distribution of mass ratios [72–74] indicates that equal-mass mergers are rare. We therefore need a way to extend Eq. (7) to generic BHBs.

Using the same post-Newtonian analysis [51] as in [50], we can extend formula (7) to less symmetric configurations by replacing $\alpha \sin \theta$ by $|\vec{\alpha}_2^\perp - q\alpha_1^\perp|/(1+q)$ and $\alpha \cos \theta$ by $2[\alpha_2^z + q^2\alpha_1^z]/(1+q)^2$. Importantly, we are assuming that terms proportional to $|\vec{\alpha}_2^\perp - q\alpha_1^\perp|^n$ (for $n > 1$) are negligible. If this is not the case, then our expansion, which can be thought of as a Fourier sine series, would still converge, but our extension would contain errors that may not be small. For example, if a term like $(\alpha^\perp)^2\alpha^z$ were present, this would contribute to all even components of the Fourier sine series and when extending the series, we would have to take this into account. This would change the behavior of kick even in more symmetric configurations. This degeneracy in the interpretation of the sine series can be broken by examining configurations with constant α^z (while varying α^\perp) and constant α^\perp (while varying α^z). These, and other configurations, will be the subject of an upcoming paper. Our justification for not including these terms is that the higher-order α^\perp terms are small in the “superkick” configuration. Furthermore, the accuracy with which formula (7) predicts the results of our $\alpha = 0.91$ simulations supports the conclusion that these terms remain small. This can be verified by confirming that formula (7) is accurate for all θ and α (a subject of our ongoing analysis that will be reported in a forthcoming paper). We emphasize that the proposed extension is an ansatz, that while reasonable as a starting point for the modeling, needs to be thoroughly

tested and refined.

Our new ansatz for the recoil velocity modifies Eq. (3) by changing the “superkick” v_{\parallel} term. The ansatz has the form (after dropping terms that previous studies indicated were small [50]):

$$\begin{aligned} \vec{V}_{\text{recoil}}(q, \vec{\alpha}) &= v_m \hat{e}_1 + v_{\perp} (\cos \xi \hat{e}_1 + \sin \xi \hat{e}_2) + v_{\parallel} \hat{n}_{\parallel}, \\ v_m &= A_m \frac{\eta^2(1-q)}{(1+q)} [1 + B_m \eta], \\ v_{\perp} &= H \frac{\eta^2}{(1+q)} \left[(\alpha_2^{\parallel} - q\alpha_1^{\parallel}) \right], \\ v_{\parallel} &= 16\eta^2/(1+q) \left[V_{1,1} + V_A \tilde{S}_z + V_B \tilde{S}_z^2 + V_C \tilde{S}_z^3 \right] \\ &\quad \times |\vec{\alpha}_2^{\perp} - q\vec{\alpha}_1^{\perp}| \cos(\phi_{\Delta} - \phi_1), \end{aligned} \quad (12)$$

where $\tilde{S} = 2(\vec{\alpha}_2 + q^2\vec{\alpha}_1)/(1+q)^2$, and the coefficients we use in the statistical studies below are $H = 6.9 \times 10^3$ [48], $A_m = 1.2 \times 10^4$, $B_m = -0.93$ [12], and the remaining coefficients are obtained from Eq. (7) above.

VII. STATISTICAL STUDIES

Using Eq. (12) and the above fitted spin magnitude (α), and direction distributions (θ), the mass ratio distribution suggested in [72–74], $P(q) \propto q^{-0.3}(1-q)$, and assuming that the two BHs can have arbitrary orientations for the in-plane component of the spin (i.e. uniform probability in the range $0 \leq \phi \leq 2\pi$), we obtain probabilities for the recoil velocity magnitude and direction. To perform our statistical studies, we choose 10^8 configurations (2×10^8 configurations in total) randomly chosen based on the above probability distributions and examine the predicted recoil magnitude and direction. Our results are summarized in Table VIII and Figs. 9 and 10. Although we include the pure unequal mass recoil [v_m in Eq. (12)], we note that the modeling of the angle ξ as a function of the binary’s parameter is incomplete. However v_m has normally a nonleading effect. We therefore chose a constant $\xi = 145^\circ$, as suggested in our previous study [48].

In Fig. 11 we show the probabilities that the recoil has a given inclination angle (angle with respect to the orbital angular momentum) for hot and cold disks. Because of the $\theta \rightarrow 180^\circ - \theta$ symmetry, we map all recoil angles to the interval $0^\circ \leq \theta \leq 90^\circ$. Here $P(\theta)$ is the probability integrating over all possible recoil magnitudes, i.e. $P(\theta) = \int_0^\infty P(\theta, v) dv$. The distribution is normalized such that $\int_0^{90} P(\theta) d\theta = 1$. The angular distribution is broader for accretion in cold disks, since that tends to suppress the “hangup-kick” and “superkick”, while the distribution is more sharply peaked near $\theta = 0$ for hot disks.

This strong angular dependence of the recoil has particular relevance for the studies of the observational con-

TABLE VIII: Recoil velocity probabilities (in percent) for BHs in hot and cold disks aligned binaries and the probabilities for the recoil along the line-of-sight having the given magnitude range (denoted by Obs.). For the hot case, there is a nontrivial probability of observing a recoil larger than 2000 km s^{-1} , but for cold disks, such recoils are suppressed. Velocities are in units of km s^{-1} .

Vel. (km s^{-1})	(Hot)	Obs. (Hot)	(Cold)	Obs. (Cold)
0-100	34.2593 %	60.1847 %	41.4482 %	71.2967 %
100-200	21.1364 %	16.9736 %	28.3502 %	16.8471 %
200-300	11.6901 %	8.1110 %	12.503 %	6.1508 %
300-400	7.8400 %	4.8108 %	7.0967 %	2.8281 %
400-500	5.7590 %	3.0913 %	4.2490 %	1.3973 %
500-1000	14.0283 %	5.6593 %	5.9309 %	1.4258 %
1000-1500	4.0183 %	0.9809 %	0.4030 %	0.0526 %
1500-2000	1.0309 %	0.1638 %	0.0185 %	0.0015 %
2000-2500	0.2047 %	0.0223 %	0.0005 %	$2 \times 10^{-5}\%$
2500-3000	0.0296 %	0.0023 %	$1 \times 10^{-5}\%$	0.0%
3000-3500	0.0032 %	0.0002 %	0.0%	0.0%
3500-4000	0.0002 %	$4. \times 10^{-6}\%$	0.0%	0.0%

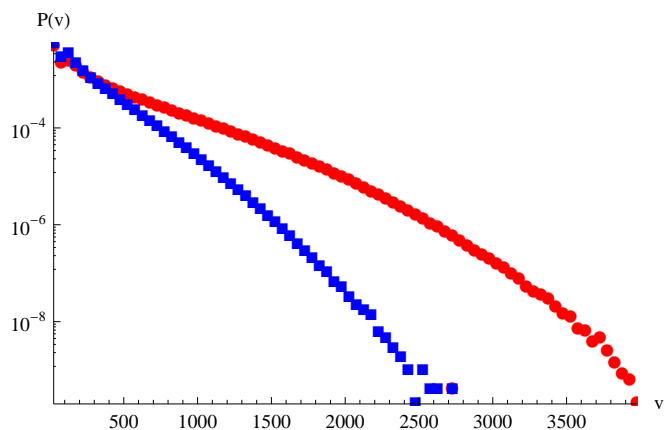


FIG. 9: Probability distribution $P(v)$ of the recoil magnitude for BHBs alignment configurations in hot (top curve, red circles) and cold disks BHBs (lower curve, blue squares). The velocity is in units of km s^{-1} .

sequences of merging and kicked BHs surrounded by pre-existing gas disks [19, 75–80]. The merger of a BHB resulting in the remnant BH moving across the matter that surrounded the original BHB would greatly affect the dynamics of the gas and its thermodynamic state. This translates into distinctive electromagnetic signatures that could reveal the presence of recoiling BHs. The effect is very pronounced when the BH recoils in the orbital plane with a large magnitude. The strong preference for large recoils along the axis of the disk over those recoiling along the disk itself can strongly suppress the magnitude of such signatures.

In Fig. 12 we show the recoil velocity distribution for hot and cold disks integrated over 15° intervals of the inclination angle θ (in Figs. 9 and 10 above, the integration is over $0^\circ \leq \theta \leq 180^\circ$). While in Fig. 13, we show the integrated probability, $\Pi(v)$ of a recoil having velocity

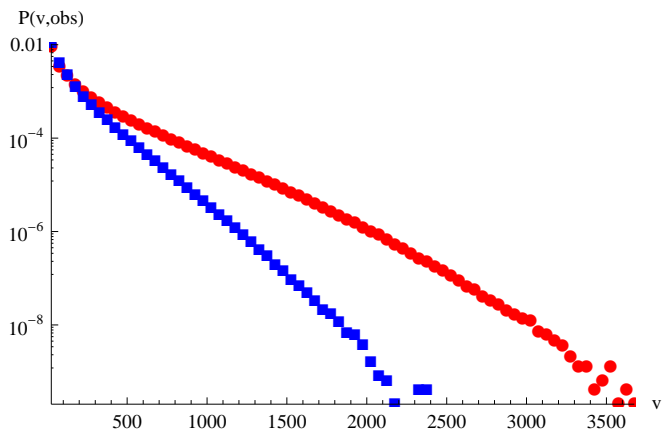


FIG. 10: Probability distribution $P(v)$ of the recoil magnitude along the line of sight for BHBs in hot (top curve, red circles) and cold disks (lower curve, blue squares). The velocity is in units of km s^{-1} .

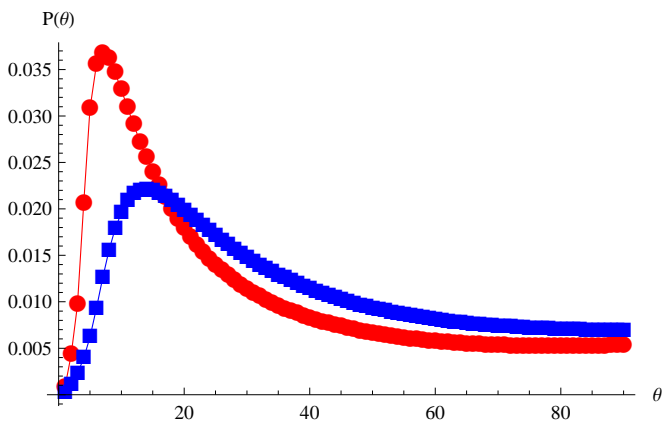


FIG. 11: The probability distribution of the inclination angle θ of the recoil (measured with respect to the axis of the angular momentum) for hot (narrower distribution, red circles) and cold environments (blue squares). Angles are measured in degrees. Note that $P(180^\circ - \theta) = P(\theta)$. These distributions were created by mapping $\theta \rightarrow 180^\circ - \theta$ for $\theta > 90^\circ$.

v or larger [$\Pi(v) = \int_v^\infty P(\nu) d\nu$]. If we consider recoils within 15° of the orbital axis, we see that velocities up to 900 km s^{-1} are likely (i.e. about 1% probability) for cold disks and up to 1600 km s^{-1} for hot disks (see also Fig. 13). If we look at angles between 15° and 30° we see the recoils are limited to less than 800 km s^{-1} (even for hot disks, a recoil of 600 km s^{-1} has $< 0.1\%$ probability). At larger θ angles, the maximum recoil drops below 270 km s^{-1} .

Since the most striking effects are likely due to BHs recoiling with large magnitudes through the plane of the disk, it is interesting to examine the probabilities of such events occurring. Even with integrated probabilities of $\lesssim 10^{-4}$, such events may be observed in large surveys of galaxies, e.g. the Sloan Digital Sky Survey DR7 contains $\sim 9 \times 10^5$ galaxies if the observable ef-

TABLE IX: Recoil velocity direction (θ) probabilities for the hot and cold cases. Recoils with $\theta > 90^\circ$ have been remapped using the symmetry $\theta \rightarrow 180^\circ - \theta$.

Range	(Hot)	(Cold)
$0^\circ - 30^\circ$	61.6%	47.0%
$30^\circ - 60^\circ$	22.6%	31.4%
$60^\circ - 90^\circ$	15.7%	21.6%

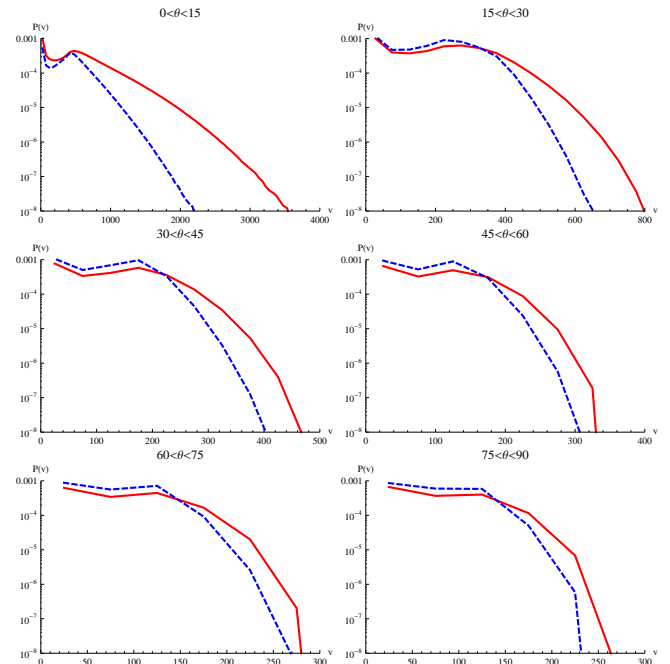


FIG. 12: Recoil velocity distributions for hot (red solid lines) and cold (blue dashed lines) disks for recoils in angular intervals 15 degrees wide (Eq. (12) predicts equal probabilities for recoils at an angle θ and $180^\circ - \theta$). Note how rapidly the maximum recoil decreases as a function of θ . Recoils as large as 1000 km s^{-1} must have $\theta < 15^\circ$ and in-plane recoils are less than 270 km s^{-1} (but see comment about unequal-mass recoils in the text).

fects last long enough. We can see in Figs. 12 and 13 that while in hot disks we can observe recoils of nearly 3000 km s^{-1} , cold disks limit the maximum observable recoil to 2000 km s^{-1} . On the other end, if we require the recoiling hole to be within 30° of the orbital plane (i.e. $\theta > 60^\circ$) we cannot observe recoils larger than 250 km s^{-1} , while at intermediate angles velocities seem limited to 400 km s^{-1} for both cold and hot disks.

In Fig. 14, we show the angular distribution for recoils in given velocity ranges. Again, because of the $\theta \rightarrow 180^\circ - \theta$ symmetry, we map all recoil angles to the interval $0 \leq \theta \leq 90^\circ$. For convenience, we plot the probabilities in degrees rather than radians. For these plots, we used 10^8 randomly chosen binaries consistent with the above distributions for spin magnitude, spin direction, and mass ratio. The maximum angle the recoil can make with the orbital angular momentum axis is very

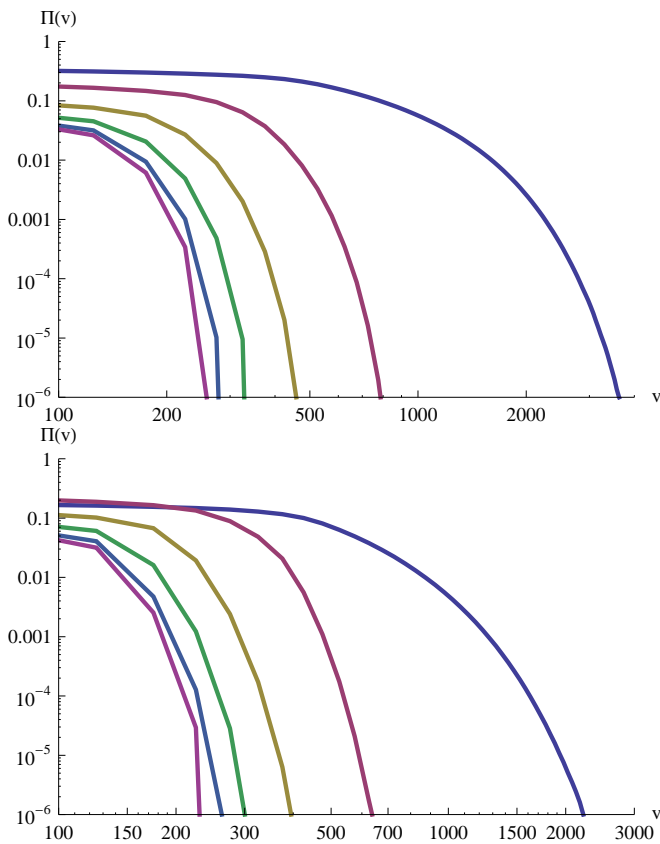


FIG. 13: The integrated probability $\Pi(v)$ of a recoil having velocity v or larger [$\Pi(v) = \int_v^\infty P(\nu)d\nu$] for hot (top) and cold (bottom) accretion disks for recoils in the ranges $0^\circ < \theta < 15^\circ$, $15^\circ < \theta < 30^\circ$, \dots , $75^\circ < \theta < 90^\circ$. In both cases, for recoils larger than 200 km s^{-1} , the recoil probabilities are smaller for larger values of θ . In the cold case, low-velocity ($< 200 \text{ km s}^{-1}$) recoils with an angle $0^\circ < \theta < 15^\circ$ are less probable than recoils with angle $15^\circ < \theta < 30^\circ$.

restrictive for large velocities, as is shown in Table X.

VIII. DISCUSSION

We studied in detail a family of BHB configurations with full numerical relativity that allowed us to single out the “hangup-kick”. This effect is expected to be relevant in generic BBH mergers since it arises from a combination of generic properties of the orbital dynamics of spinning BHBs, namely the “orbital-hangup effect” [81] and the “superkick effect” [16]. We present evidence that this effect increases the maximum recoil velocity achievable from the merger of two orbiting BHs by up to 1200 km s^{-1} with respect to previous estimates, approaching nearly 5000 km s^{-1} . Even more importantly this maximum recoil is reached for spins at angles near 50° with respect to the orbital momentum of the binary system. We have also shown evidence that accretion in the premerger stage of the binary tends to align spins with the angular momentum of the system, leading to

TABLE X: Maximum recoil angle θ (angle with respect to the orbital angular momentum axis) for given recoil velocity ranges. Note here that $\theta_{\text{max}} < \delta$ means that θ must smaller than δ or larger than $180^\circ - \delta$.

Range	θ_{max} (Hot)	θ_{max} (Cold)
$0 - 100 \text{ km s}^{-1}$	90°	90°
$100 - 200 \text{ km s}^{-1}$	90°	90°
$200 - 300 \text{ km s}^{-1}$	$< 80^\circ$	$< 70^\circ$
$300 - 400 \text{ km s}^{-1}$	$< 45^\circ$	$< 40^\circ$
$400 - 500 \text{ km s}^{-1}$	$< 33^\circ$	$< 30^\circ$
$500 - 600 \text{ km s}^{-1}$	$< 25^\circ$	$< 21^\circ$
$500 - 1000 \text{ km s}^{-1}$	$< 25^\circ$	$< 21^\circ$
$1000 - 1500 \text{ km s}^{-1}$	$< 11^\circ$	$< 8^\circ$
$1500 - 2000 \text{ km s}^{-1}$	$< 7^\circ$	$< 5^\circ$
$2000 - 2500 \text{ km s}^{-1}$	$< 5^\circ$	$< 4^\circ$
$2500 - 3000 \text{ km s}^{-1}$	$< 4^\circ$	$< 2^\circ$
$3000 - 3500 \text{ km s}^{-1}$	$< 3^\circ$	***

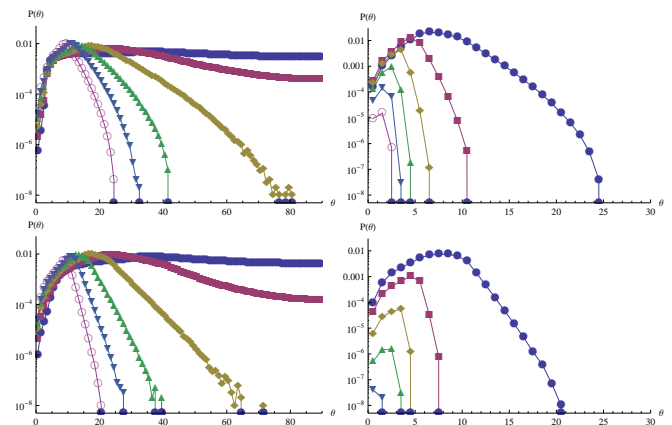


FIG. 14: Recoil angle probabilities $P(\theta)$ for hot (top) and cold (bottom) disks aligned binaries. The plots on the left show angular probabilities for velocities in the ranges $0 - 100 \text{ km s}^{-1}$, $100 - 200 \text{ km s}^{-1}$, \dots , $500 - 600 \text{ km s}^{-1}$. The plots on the right show $P(\theta)$ for velocity ranges of $500 - 1000 \text{ km s}^{-1}$, \dots , $3000 - 3500 \text{ km s}^{-1}$. Probabilities for θ and $180^\circ - \theta$ are equal. In the plots, closed circles correspond to the smallest range, followed by squares, diamonds, triangles (vertex up), triangles (vertex down), and open circles. The circles on the axis are an artifact of the visualization tool.

distributions that favor the “hangup-kick” configurations with respect to the purely in-plane “superkick” ones. Due to depletion of nearby matter, the merger itself occurs in a “dry” regime where accretion no longer affects the BH spins.

In an attempt to estimate the probability of observing such large recoils in real astronomical systems, we assumed accretion driven distributions for the spin magnitudes and directions, based on the two extreme scenarios of cold and hot disks, and assumed a mass ratio distribution based on independent estimates, to obtain non negligible probabilities of observing recoils of several thousand km s^{-1} . In particular, the results in Table VIII indicate that surveys exploring peculiar differential radial

velocities should observe at least one case of a “line-of-sight” velocity above 2000 km s^{-1} out of four thousand merged galaxies (assuming “hot” disks). The probability that a remnant BH receives a recoil exceeding the escape velocity (in any direction) of giant galaxies (2000 km s^{-1}) is ten times larger. Probabilities of recoils exceeding the escape velocity quickly rise to 5% for galaxies with escape velocities of 1000 km s^{-1} and nearly 20% for galaxies with escape velocities of 500 km s^{-1} . These numbers indicate that recoil velocities and modeling the accretion of the supermassive BHs in centers of galaxies should be important ingredients in understanding the growth of supermassive BHs and large scale structure formation in the universe.

Our initial study showed the relevance of recoil and accretion modeling in order to better understand how BHs evolve and grow in the universe. There are several aspects that deserve further study. The recoil formula needs to be further tested and developed in the intermediate mass ratio regime and for fully precessing BHs. Accretion needs to be modeled at even smaller scales, i.e. at sub-milli-parsecs. In between the accretion regime governed by Newtonian physics and the fully nonlinear regime, a slow adiabatic inspiral occurs. This intermediate regime can be described by semianalytic methods, such as the post-Newtonian approximations. It has been pointed out that resonances for certain mass ratios can lead to further spin alignment [82, 83] and hence change

the initial spin distributions used in the applications of the recoil formula (12). Further theoretical and observational explorations of the recoil phenomena are well worth being pursued since they could represent the first prediction and verification of General Relativity in its most highly dynamical and nonlinear regime.

Acknowledgments

The authors thank M.Favata and V.Paschalidis for pointing out Ref. [45] and T. Bogdanovic and C. Miller for careful reading of the manuscript. CL and YZ gratefully acknowledge the NSF for financial support from Grants AST-1028087, PHY-0929114, PHY-0969855, PHY-0903782, OCI-0832606, and DRL-1136221, and NASA for financial support from NASA Grant No. 07-ATFP07-0158. Computational resources were provided by the Ranger system at the Texas Advance Computing Center (Teragrid allocation TG-PHY060027N), which is supported in part by the NSF, and by NewHorizons at Rochester Institute of Technology, which was supported by NSF grant No. PHY-0722703, DMS-0820923 and AST-1028087. MV acknowledges the NSF for financial support from NSF award AST-1107675.

-
- [1] M. C. Begelman, R. D. Blandford, and M. J. Rees, *Reviews of Modern Physics* **56**, 255 (1984).
 - [2] I. H. Redmount and M. J. Rees, *Comments on Astrophysics* **14**, 165 (1989).
 - [3] L. Blecha, T. J. Cox, A. Loeb, and L. Hernquist, *MNRAS* **412**, 2154 (2011), 1009.4940.
 - [4] M. J. Fitchett, *MNRAS* **203**, 1049 (1983).
 - [5] M. J. Fitchett and S. Detweiler, *Mon. Not. R. astr. Soc.* **211**, 933 (1984).
 - [6] L. Blanchet, M. S. S. Qusailah, and C. M. Will, *Astrophys. J.* **635**, 508 (2005), astro-ph/0507692.
 - [7] A. Le Tiec, L. Blanchet, and C. M. Will, *Class. Quant. Grav.* **27**, 012001 (2010), 0910.4594.
 - [8] M. Campanelli, *Class. Quant. Grav.* **22**, S387 (2005), astro-ph/0411744.
 - [9] F. Pretorius, *Phys. Rev. Lett.* **95**, 121101 (2005), gr-qc/0507014.
 - [10] M. Campanelli, C. O. Lousto, P. Marronetti, and Y. Zlochower, *Phys. Rev. Lett.* **96**, 111101 (2006), gr-qc/0511048.
 - [11] J. G. Baker, J. Centrella, D.-I. Choi, M. Koppitz, and J. van Meter, *Phys. Rev. Lett.* **96**, 111102 (2006), gr-qc/0511103.
 - [12] J. A. González, U. Sperhake, B. Brügmann, M. Hannam, and S. Husa, *Phys. Rev. Lett.* **98**, 091101 (2007), gr-qc/0610154.
 - [13] F. Herrmann, I. Hinder, D. Shoemaker, P. Laguna, and R. A. Matzner, *Astrophys. J.* **661**, 430 (2007), gr-qc/0701143.
 - [14] M. Koppitz, D. Pollney, C. Reisswig, L. Rezzolla, J. Thornburg, et al., *Phys. Rev. Lett.* **99**, 041102 (2007), gr-qc/0701163.
 - [15] M. Campanelli, C. O. Lousto, Y. Zlochower, and D. Merritt, *Astrophys. J.* **659**, L5 (2007), gr-qc/0701164.
 - [16] M. Campanelli, C. O. Lousto, Y. Zlochower, and D. Merritt, *Phys. Rev. Lett.* **98**, 231102 (2007), gr-qc/0702133.
 - [17] C. O. Lousto and Y. Zlochower, *Phys. Rev. Lett.* **107**, 231102 (2011), 1108.2009.
 - [18] S. Komossa, H. Zhou, and H. Lu, *Astrop. J. Letters* **678**, L81 (2008), 0804.4585.
 - [19] G. A. Shields and E. W. Bonning, *Astrophys. J.* **682**, 758 (2008), 0802.3873.
 - [20] T. Bogdanovic, M. Eracleous, and S. Sigurdsson, *Astrophys. J.* **697**, 288 (2009), 0809.3262.
 - [21] F. Civano et al., *Astrophys. J.* **717**, 209 (2010), 1003.0020.
 - [22] M. Eracleous, T. A. Boroson, J. P. Halpern, and J. Liu (2011), 1106.2952.
 - [23] P. Tsalmantza, R. Decarli, M. Dotti, and D. W. Hogg, *Astrophys. J.* **738**, 20 (2011), 1106.1180.
 - [24] T. Bogdanovic, C. S. Reynolds, and M. C. Miller, *Astrophys. J.* **661**, L147 (2007), astro-ph/0703054.
 - [25] M. Dotti, M. Volonteri, A. Perego, M. Colpi, M. Ruzsowski, and F. Haardt, *mnras* **402**, 682 (2010), 0910.5729.
 - [26] M. Ansorg, B. Brügmann, and W. Tichy, *Phys. Rev. D* **70**, 064011 (2004), gr-qc/0404056.
 - [27] S. Brandt and B. Brügmann, *Phys. Rev. Lett.* **78**, 3606

- (1997), gr-qc/9703066.
- [28] Y. Zlochower, J. G. Baker, M. Campanelli, and C. O. Lousto, *Phys. Rev.* **D72**, 024021 (2005), gr-qc/0505055.
- [29] P. Marronetti, W. Tichy, B. Brüggmann, J. Gonzalez, and U. Sperhake, *Phys. Rev.* **D77**, 064010 (2008), 0709.2160.
- [30] C. O. Lousto and Y. Zlochower, *Phys. Rev.* **D77**, 024034 (2008), 0711.1165.
- [31] Cactus Computational Toolkit home page: <http://cactuscode.org>.
- [32] Einstein Toolkit home page: <http://einsteintoolkit.org>.
- [33] E. Schnetter, S. H. Hawley, and I. Hawke, *Class. Quantum Grav.* **21**, 1465 (2004), gr-qc/0310042.
- [34] M. Alcubierre, B. Brüggmann, P. Diener, M. Koppitz, D. Pollney, E. Seidel, and R. Takahashi, *Phys. Rev.* **D67**, 084023 (2003), gr-qc/0206072.
- [35] J. R. van Meter, J. G. Baker, M. Koppitz, and D.-I. Choi, *Phys. Rev.* **D73**, 124011 (2006), gr-qc/0605030.
- [36] J. Thornburg, *Class. Quant. Grav.* **21**, 743 (2004), gr-qc/0306056.
- [37] O. Dreyer, B. Krishnan, D. Shoemaker, and E. Schnetter, *Phys. Rev.* **D67**, 024018 (2003), gr-qc/0206008.
- [38] M. Campanelli and C. O. Lousto, *Phys. Rev.* **D59**, 124022 (1999), gr-qc/9811019.
- [39] C. O. Lousto and Y. Zlochower, *Phys. Rev.* **D76**, 041502(R) (2007), gr-qc/0703061.
- [40] C. O. Lousto and Y. Zlochower, *Phys. Rev.* **D83**, 024003 (2011), 1011.0593.
- [41] H. P. Pfeiffer et al., *Class. Quant. Grav.* **24**, S59 (2007), gr-qc/0702106.
- [42] A. Buonanno, L. E. Kidder, A. H. Mroue, H. P. Pfeiffer, and A. Taracchini, *Phys. Rev.* **D83**, 104034 (2011), 1012.1549.
- [43] M. Campanelli, C. O. Lousto, Y. Zlochower, B. Krishnan, and D. Merritt, *Phys. Rev.* **D75**, 064030 (2007), gr-qc/0612076.
- [44] M. Campanelli, C. O. Lousto, and Y. Zlochower, *Phys. Rev.* **D74**, 084023 (2006), astro-ph/0608275.
- [45] D. A. Nichols and Y. Chen, *Phys. Rev. D* (2011), 1109.0081.
- [46] C. O. Lousto and Y. Zlochower, *Phys. Rev.* **D79**, 064018 (2009), 0805.0159.
- [47] S. Dain, C. O. Lousto, and Y. Zlochower, *Phys. Rev.* **D78**, 024039 (2008), 0803.0351.
- [48] C. O. Lousto and Y. Zlochower, *Phys. Rev.* **D77**, 044028 (2008), 0708.4048.
- [49] L. E. Kidder, *Phys. Rev.* **D52**, 821 (1995), gr-qc/9506022.
- [50] C. O. Lousto, M. Campanelli, Y. Zlochower, and H. Nakano, *Class. Quant. Grav.* **27**, 114006 (2010), 0904.3541.
- [51] E. Racine, A. Buonanno, and L. E. Kidder, *Phys. Rev.* **D80**, 044010 (2009), 0812.4413.
- [52] Y. Zlochower, M. Campanelli, and C. O. Lousto, *Class. Quant. Grav.* **28**, 114015 (2011), 1011.2210.
- [53] L. Boyle and M. Kesden, *Phys. Rev.* **D78**, 024017 (2008), 0712.2819.
- [54] F. Herrmann, I. Hinder, D. M. Shoemaker, P. Laguna, and R. A. Matzner, *Phys. Rev.* **D76**, 084032 (2007), 0706.2541.
- [55] C. O. Lousto, H. Nakano, Y. Zlochower, and M. Campanelli, *Phys. Rev.* **D81**, 084023 (2010), 0910.3197.
- [56] L. Mayer, S. Kazantzidis, P. Madau, M. Colpi, T. Quinn, and J. Wadsley, *Science* **316**, 1874 (2007), 0706.1562.
- [57] P. F. Hopkins and E. Quataert, *MNRAS* **407**, 1529 (2010), 0912.3257.
- [58] D. Downes and P. M. Solomon, *ApJ* **507**, 615 (1998), arXiv:astro-ph/9806377.
- [59] R. I. Davies, L. J. Tacconi, and R. Genzel, *ApJ* **613**, 781 (2004), arXiv:astro-ph/0406342.
- [60] R. I. Davies, L. J. Tacconi, and R. Genzel, *ApJ* **602**, 148 (2004), arXiv:astro-ph/0310681.
- [61] J. M. Bardeen and J. A. Petterson, *ApJ* **195**, L65+ (1975).
- [62] A. Perego, M. Dotti, M. Colpi, and M. Volonteri, *mnras* **399**, 2249 (2009), 0907.3742.
- [63] S. L. Shapiro and S. A. Teukolsky, *Black Holes, White Dwarfs, and Neutron Stars* (John Wiley & Sons, New York, 1983).
- [64] Y. Springel, N. Yoshida, and S. D. M. White, *New Astronomy* **6**, 79 (2001), astro-ph/0003162.
- [65] M. Dotti, M. Ruzszkowski, L. Paredi, M. Colpi, M. Volonteri, and F. Haardt, *MNRAS* **396**, 1640 (2009), 0902.1525.
- [66] M. Spaans and J. Silk, *ApJ* **538**, 115 (2000), arXiv:astro-ph/0002483.
- [67] R. S. Klessen, M. Spaans, and A. Jappsen, *MNRAS* **374**, L29 (2007), arXiv:astro-ph/0610557.
- [68] M. Dotti, M. Colpi, and F. Haardt, *MNRAS* **367**, 103 (2006).
- [69] M. Dotti, M. Colpi, F. Haardt, and L. Mayer, *MNRAS* **379**, 956 (2007), arXiv:astro-ph/0612505.
- [70] N. I. Shakura and R. A. Sunyaev, *A&A* **24**, 337 (1973).
- [71] G. Lodato and J. E. Pringle, *MNRAS* **381**, 1287 (2007), 0708.1124.
- [72] Q. Yu, Y. Lu, R. Mohayaee, and J. Colin, *Astrophys. J.* **738**, 92 (2011), 1105.1963.
- [73] K. R. Stewart, J. S. Bullock, E. J. Barton, and R. H. Wechsler, *Astrophys. J.* **702**, 1005 (2009), 0811.1218.
- [74] P. F. Hopkins, K. Bundy, D. Croton, L. Hernquist, D. Keres, et al., *Astrophys. J.* **715**, 202 (2009), 0906.5357.
- [75] M. Ponce, J. A. Faber, and J. Lombardi, *James C., Astrophys. J.* **745**, 71 (2012), 1107.1711.
- [76] Z. Lippai, Z. Frei, and Z. Haiman, *Astrophys. J. Lett.* **676**, L5 (2008), 0801.0739.
- [77] E. M. Rossi, G. Lodato, P. Armitage, J. Pringle, and A. King, *Mon. Not. Roy. Astron. Soc.* **401**, 2021 (2010), 0910.0002.
- [78] L. R. Corrales, Z. Haiman, and A. MacFadyen (2009), 0910.0014.
- [79] M. Milosavljevic and E. Phinney, *Astrophys. J.* **622**, L93 (2005), astro-ph/0410343.
- [80] J. D. Schnittman and J. H. Krolik, *Astrophys. J.* **684**, 835 (2008), 0802.3556.
- [81] M. Campanelli, C. O. Lousto, and Y. Zlochower, *Phys. Rev.* **D74**, 041501(R) (2006), gr-qc/0604012.
- [82] J. D. Schnittman, *Phys. Rev.* **D70**, 124020 (2004), astro-ph/0409174.
- [83] M. Kesden, U. Sperhake, and E. Berti, *Astrophys. J.* **715**, 1006 (2010), 1003.4993.
- [84] The code computes the density of each SPH particle averaging over $N_{\text{neigh}} = 32$ neighbors.